Department of Radio Science and Engineering

Millimetre and submillimetre wave antenna design using ray tracing

Aki Karttunen

Aalto University

DOCTORAL DISSERTATIONS

Aalto University publication series
DOCTORAL DISSERTATIONS 127/2013

Millimetre and submillimetre wave antenna design using ray tracing

Aki Karttunen

A doctoral dissertation completed for the degree of Doctor of Science (Technology) to be defended, with the permission of the Aalto University School of Electrical Engineering, at a public examination held at the lecture hall S2 of the school on 10 September 2013 at 12.

Aalto University
School of Electrical Engineering
Department of Radio Science and Engineering

Supervising professor
Prof. Antti Räisänen

Thesis advisor
Dr. Juha Ala-Laurinaho

Preliminary examiners
Prof. Nuria Llombart Juan, Delft University of Technology, The Netherlands
Dr. Artem V. Boriskin, Institut d'Electronique et de Télécommunications de Rennes (IETR), France

Opponent
Prof. Andrea Neto, Delft University of Technology, The Netherlands

Aalto University publication series
DOCTORAL DISSERTATIONS 127/2013

ISBN 978-952-60-5292-2 (printed)
ISBN 978-952-60-5293-9 (pdf)
ISSN-L 1799-4934
ISSN 1799-4934 (printed)
ISSN 1799-4942 (pdf)
http://urn.fi/URN:ISBN:978-952-60-5293-9

http://lib.tkk.fi/Diss/

Unigrafia Oy
Helsinki 2013

Finland

441 697
Printed matter

Aalto University

Abstract

Aalto University, P.O. Box 11000, FI-00076 Aalto www.aalto.fi

Author
Aki Karttunen

Name of the doctoral dissertation
Millimetre and submillimetre wave antenna design using ray tracing

Publisher School of Electrical Engineering

Unit Department of Radio Science and Engineering

Series Aalto University publication series DOCTORAL DISSERTATIONS 127/2013

Field of research Radio Engineering

Manuscript submitted 6 June 2013 **Date of the defence** 10 September 2013

Permission to publish granted (date) 13 August 2013 **Language** English

☐ **Monograph** ☒ **Article dissertation (summary + original articles)**

Abstract

The millimetre and submillimetre wave frequency ranges have many current and potential applications for example in satellite technology and telecommunications. Electrically large antennas are needed in several applications, e.g., in order to achieve high antenna gain with a narrow beam. Reflector and lens antennas, with all dimensions large compared to the wavelength, are commonly designed using ray tracing. Ray tracing is based on a high frequency approximation of Maxwell's equations. The main advantage of ray tracing is the decreased computational effort as compared to more accurate full-wave methods. In this thesis, ray tracing is used in both synthesis and simulation of electrically large antennas.

In the first part of this thesis, a 650 GHz dual reflector feed system (DRFS) is designed, tested, and used in a hologram-based compact antenna test range (CATR). The DRFS provides shaped illumination that simplifies the hologram manufacturing. A ray-tracing based numerical synthesis method is used to design the 650 GHz DRFS. It is tested with antenna measurements prior to the compact range measurements. The designed DRFS is used successfully in a full scale compact range, in which a 1.5-m antenna is tested at 650 GHz.

In the second part of this thesis, several beam-steering integrated lens antennas (ILAs) are designed with ray-tracing simulations. Antenna prototypes are designed, fabricated, and tested at 77 GHz with antenna measurements. Electrical beam steering is demonstrated with integrated feed arrays and switching networks. Also, beam-steering properties of ILAs with a wide range of different lens permittivities and feed element directivities are studied with ray-tracing simulations. Lens shapes are developed for improvement of the beam properties at large beam-steering angles. With a low permittivity ILA, an intermediate eccentricity, compared to those of the conventional hemispherical and elliptical lenses, is found to have smaller scan loss and lower side-lobes with large beam-steering angles of about 30°. Placing the feeds on a spherical surface of an extended hemispherical ILA is found to result in a beam shape and gain that remain nearly constant at beam-steering angles up to about 25°. A typical disadvantage of a beam-steering ILA is the increase of the internal reflections with the increase of the feed offset. It is shown that the extension of a low permittivity extended hemispherical ILA can be shaped to significantly reduce the internal reflections. It is also shown that it is possible to design an integrated lens antenna with low reflection loss (< 1 dB), for moderate beam-steering angles (< 15°), with any lens permittivity and with any feed element directivity. The reduction of internal reflections is based on the selection of the original ellipse radius larger than the final lens radius and designing the shape of the extension for minimal reflections.

Keywords antenna measurements, beam steering, lens, ray tracing, reflector antenna

ISBN (printed) 978-952-60-5292-2 **ISBN (pdf)** 978-952-60-5293-9

ISSN-L 1799-4934 **ISSN (printed)** 1799-4934 **ISSN (pdf)** 1799-4942

Location of publisher Espoo **Location of printing** Helsinki **Year** 2013

Pages 204 **urn** http://urn.fi/URN:ISBN:978-952-60-5293-9

Aalto-yliopisto

Tiivistelmä

Aalto-yliopisto, PL 11000, 00076 Aalto www.aalto.fi

Tekijä
Aki Karttunen

Väitöskirjan nimi
Antennien suunnittelu millimetri- ja alimillimetriaaltoalueella käyttäen säteenseurantaa

Julkaisija Sähkötekniikan korkeakoulu

Yksikkö Radiotieteen ja -tekniikan laitos

Sarja Aalto University publication series DOCTORAL DISSERTATIONS 127/2013

Tutkimusala Radiotekniikka

Käsikirjoituksen pvm 06.06.2013 **Väitöspäivä** 10.09.2013

Julkaisuluvan myöntämispäivä 13.08.2013 **Kieli** Englanti

☐ **Monografia** ☒ **Yhdistelmäväitöskirja (yhteenveto-osa + erillisartikkelit)**

Tiivistelmä

Millimetri- ja alimillimetriaaltoalueilla on monia nykyisiä ja potentiaalisia sovelluskohteita, esimerkiksi satelliiteissa ja tietoliikenteessä. Sähköisesti suuria antenneja tarvitaan monissa sovelluksissa, jotta saavutettaisiin suuri antennin vahvistus ja kapea keila. Heijastin ja linssiantennit, joiden kaikki mitat ovat suuria suhteessa aallonpituuteen, suunnitellaan yleisesti käyttäen säteenseurantaa. Säteenseuranta perustuu geometriseen optiikkaan, joka on korkean taajuuden approksimaatio Maxwellin yhtälöistä. Tärkein etu säteenseurannalla suhteessa tarkempiin menetelmiin on pienempi laskennallinen kuormitus. Tässä työssä säteenseurantaa käytetään sähköisesti suurien antennien synteesiin ja simuloimiseen.

Työn ensimmäisessä osassa 650 GHz:n kaksiheijastiminen syöttöjärjestelmä suunnitellaan, testataan ja sitä käytetään hologrammiin perustuvassa antennimittapaikassa. Syöttöjärjestelmää käytetään muotoillun valaisun aikaansaamiseksi hologrammille, mikä helpottaa hologrammin valmistusta. Suunnitteluun käytetään säteenseurantaan perustuvaa numeerista synteesimenetelmää. Syöttöjärjestelmä testataan antennimittauksin ennen käyttöä. Suunniteltua syöttöjärjestelmää käytetään menestyksekkäästi täyden mittakaavan antennimittapaikassa, jossa 1,5 m:n antenni testataan 650 GHz:llä.

Työn toisessa osassa suunnitellaan säteenseurantaa käyttäen integroituja linssiantenneja. Useita antenneja suunnitellaan, valmistetaan ja testataan 77 GHz:n taajuudella. Sähköinen keilankääntö demonstroidaan käyttäen integroituja syöttöryhmiä ja kytkinverkkoja. Linssien keilankääntöominaisuuksia tutkitaan säteenseurannalla vertaillen eri permittiivisyyksiä ja syötön suuntaavuuksia. Keilankääntöominaisuuksia kehitetään muotoilemalla linssiä. Kun tarkastellaan noin 30° keilankääntöaluetta, havaitaan, että matalan permittiivisyyden linsseillä paras eksentrisyys on perinteisten jatkettujen puolipallolinssien ja elliptisten linssien eksentrisyyksien väliltä. Toisaalta, jos asetetaan syöttöantennit pallomaiselle pinnalle jatketun puolipallolinssin tapauksessa, saavutetaan keilan muoto ja vahvistus, jotka pysyvät lähes vakioina 25°:n keilankääntökulmille asti. Tyypillisesti, kun syöttöantenni on kaukana linssin optisesta polttopisteestä, syntyy merkittävästi sisäisiä heijastuksia. Työssä osoitetaan, että näitä haitallisia heijastuksia voidaan merkittävästi vähentää muotoilemalla jatketun puolipallolinssin jatkos osaa. Lisäksi osoitetaan, että on mahdollista suunnitella linssin muoto siten, että heijastuhäviö on matala (< 1 dB) kohtuullisille keilankääntökulmille saakka (< 15°) käyttäen mitä tahansa linssin permittiivisyyttä tai syötön suuntaavuutta. Heijastuhäviöiden vähentäminen perustuu siihen, että valitaan alkuperäisen ellipsin pikkuakseli lopullista linssin sädettä suuremmaksi ja että linssiä muotoillaan heijastusten minimoimiseksi.

Avainsanat antennimittaukset, keilankääntö, linssi, säteenseuranta, heijastinantenni

ISBN (painettu) 978-952-60-5292-2 **ISBN (pdf)** 978-952-60-5293-9

ISSN-L 1799-4934 **ISSN (painettu)** 1799-4934 **ISSN (pdf)** 1799-4942

Julkaisupaikka Espoo **Painopaikka** Helsinki **Vuosi** 2013

Sivumäärä 204 **urn** http://urn.fi/URN:ISBN:978-952-60-5293-9

Preface

Special thanks to my supervisor Antti Räisänen and instructor Juha Ala-Laurinaho for giving me interesting research topics and for your help in proofreading this thesis. I would like to thank the whole hologram CATR team with special thanks to my master's thesis instructor Janne Häkli. Merci Ronan! Your comments and observations have always been useful.

Thanks to Janne, Aleksi, Risto, Viktor, Rummis, Eikka, Matti, Jussi, Antti, and many others. Special thanks to 3k!

Tahdon myös kiittää Saria, Miiaa, Raijaa, Teuvoa ja Reettaa tuesta ja kannustuksesta. Lämpimät kiitokset kaikille Huhmislaisille.

Espoo, August 14, 2013,

Aki Karttunen

Contents

List of Publications

This thesis consists of an overview and of the following publications which are referred to in the text by their Roman numerals.

I A. Karttunen, J. Häkli, and A. V. Räisänen, "Design of a 650 GHz dual reflector feed system for a hologram-based CATR," *European Conference on Antennas and Propagation (EuCAP)*, Nice, France, paper 359216, Nov. 6–10, 2006.

II A. Karttunen, M. Vaaja, and A. V. Räisänen, "Antenna measurement at 650 GHz with a planar near-field scanner," *Proceedings of the 29th Annual Meeting & Symposium of the Antenna Measurement Techniques Association (AMTA)*, St. Louis, MO, USA, pp. 330–336, Nov. 4–9, 2007.

III A. Karttunen, J. Ala-Laurinaho, M. Vaaja, T. Koskinen, J. Häkli, A. Lönnqvist, J. Mallat, A. Tamminen, V. Viikari, and A. V. Räisänen, "Antenna tests with a hologram-based CATR at 650 GHz," *IEEE Transactions on Antennas and Propagation*, vol. 57, no. 3, pp. 711–720, Mar. 2009.

IV A. Karttunen, J. Ala-Laurinaho, R. Sauleau, and A. V. Räisänen, "A study of extended hemispherical lenses for a high-gain beam-steering antenna," *European Conference on Antennas and Propagation (EuCAP)*, Barcelona, Spain, p. A25-1/1842008, Apr. 12–16, 2010.

V J. Ala-Laurinaho, A. Karttunen, J. Säily, A. Lamminen, R. Sauleau, and A. V. Räisänen, "Mm-wave lens antenna with an integrated LTCC feed

array for beam steering," *European Conference on Antennas and Propagation (EuCAP)*, Barcelona, Spain, p. C09P1-2/1841151, Apr. 12–16, 2010.

VI A. Karttunen, J. Ala-Laurinaho, R. Sauleau, and A. V. Räisänen, "Optimal eccentricity of a low permittivity integrated lens for a high-gain beam-steering antenna," *European Conference on Antennas and Propagation (EuCAP)*, Rome, Italy, pp. 3522–3526, Apr. 11–15, 2011.

VII A. Karttunen, J. Säily, A. Lamminen, J. Ala-Laurinaho, R. Sauleau, and A. V. Räisänen, "Using optimized eccentricity Rexolite lens for electrical beam steering with integrated aperture coupled patch array," *Progress In Electromagnetics Research B*, vol. 44, pp. 345–365, 2012.

VIII A. Karttunen, J. Ala-Laurinaho, R. Sauleau, and A. V. Räisänen, "Reduction of internal reflections in low permittivity integrated lens antennas," *Millimetre Wave Days*, Espoo, Finland, May 23–25, 2011.

IX A. Karttunen, J. Ala-Laurinaho, R. Sauleau, and A. V. Räisänen, "Extended hemispherical integrated lens antenna with feeds on a spherical surface," *European Conference on Antennas and Propagation (EuCAP)*, Gothenburg, Sweden, pp. 2463–2467, 8–12 Apr. 2013.

X A. Karttunen, J. Ala-Laurinaho, R. Sauleau, and A. V. Räisänen, "2D beam-steering with non-symmetrical beam using non-symmetrical integrated lens antenna," *European Conference on Antennas and Propagation (EuCAP)*, Prague, Czech Republic, pp. 2976–2980, Mar. 25–30, 2012.

XI A. Karttunen, J. Ala-Laurinaho, R. Sauleau, and A. V. Räisänen, "Reduction of internal reflections in integrated lens antennas for beam-steering," *Progress In Electromagnetics Research*, vol. 134, pp. 63–78, 2013.

Author's Contribution

Publication I: "Design of a 650 GHz dual reflector feed system for a hologram-based CATR"

The author designed the antenna, conducted the simulations, and prepared the publication. Dr. Janne Häkli and Prof. Antti Räisänen supervised the work.

Publication II: "Antenna measurement at 650 GHz with a planar near-field scanner"

The author had the main idea and conducted the antenna measurements. The author prepared the publication. Prof. Antti Räisänen supervised the work.

Publication III: "Antenna tests with a hologram-based CATR at 650 GHz"

The paper is a result of collaborative work. The author had the main responsibility in writing the publication. He designed and tested the dual reflector feed system. The author contributed to the preparation and execution of the antenna testing. He had the main responsibility in analyzing the results and conducted the simulations of the antenna under test.

Publication IV: "A study of extended hemispherical lenses for a high-gain beam-steering antenna"

The author had the main idea, conducted the simulations, and prepared the publication. Dr. Juha Ala-Laurinaho, Prof. Ronan Sauleau, and Prof. Antti Räisänen supervised the work.

Publication V: "Mm-wave lens antenna with an integrated LTCC feed array for beam steering"

The paper is a result of collaborative work. The author designed the lens antenna, and conducted the lens antenna simulations and measurements. Dr. Juha Ala-Laurinaho had the main responsibility in writing the publication. Dr. Jussi Säily and Mr. Antti Lamminen designed the feed array and the switching array. Prof. Ronan Sauleau and Prof. Antti Räisänen supervised the work.

Publication VI: "Optimal eccentricity of a low permittivity integrated lens for a high-gain beam-steering antenna"

The author had the main idea, conducted the simulations, and prepared the publication. Dr. Juha Ala-Laurinaho, Prof. Ronan Sauleau, and Prof. Antti Räisänen supervised the work.

Publication VII: "Using optimized eccentricity Rexolite lens for electrical beam steering with integrated aperture coupled patch array"

The paper is a result of collaborative work. The author designed the lens antenna, conducted the lens antenna simulations and measurements, and had the main responsibility in writing the publication. Dr. Jussi Säily and Mr. Antti Lamminen designed the feed array and the switching array. Dr. Juha Ala-Laurinaho, Prof. Ronan Sauleau, and Prof. Antti Räisänen supervised the work.

Publication VIII: "Reduction of internal reflections in low permittivity integrated lens antennas"

The author had the main idea, designed the antennas, conducted the simulations and measurements, and prepared the publication. Dr. Juha Ala-Laurinaho, Prof. Ronan Sauleau, and Prof. Antti Räisänen supervised the work.

Publication IX: "Extended hemispherical integrated lens antenna with feeds on a spherical surface"

The author had the main idea, designed the antennas, conducted the measurements and simulations, and prepared the publication. Dr. Juha Ala-Laurinaho, Prof. Ronan Sauleau, and Prof. Antti Räisänen supervised the work.

Publication X: "2D beam-steering with non-symmetrical beam using non-symmetrical integrated lens antenna"

The author had the main idea, designed the antennas, conducted the simulations and measurements, and prepared the publication. Dr. Juha Ala-Laurinaho, Prof. Ronan Sauleau, and Prof. Antti Räisänen supervised the work.

Publication XI: "Reduction of internal reflections in integrated lens antennas for beam-steering"

The author had the main idea, designed the antennas, conducted the simulations, and prepared the publication. Dr. Juha Ala-Laurinaho, Prof. Ronan Sauleau, and Prof. Antti Räisänen supervised the work.

List of symbols

a	ellipse semimajor axis [m]
A	area [m^2]
A_{cross}	ray tube cross-sectional area [m^2]
b	ellipse semiminor axis [m]
c_0	speed of light in free space [m/s]
C	ray length constant [m]
e	eccentricity
$\overline{E}$	electric field strength [V/m]
$\overline{E}_0$	0^{th} order term of electric field strength [V/m]
E_1	incident electric field strength [V/m]
E_1'	reflected electric field strength [V/m]
E_2'	refracted electric field strength [V/m]
$E_1^{\parallel}$	parallel polarisation of incident electric field strength [V/m]
$E_1'^{\parallel}$	parallel polarisation of reflected electric field strength [V/m]
$E_2'^{\parallel}$	parallel polarisation of refracted electric field strength [V/m]
$E_1^{\perp}$	perpendicular polarisation of incident electric field strength [V/m]
$E_1'^{\perp}$	perpendicular polarisation of reflected electric field strength [V/m]
$E_2'^{\perp}$	perpendicular polarisation of refracted electric field strength [V/m]
$\overline{E}_i$	i^{th} order term of electric field strength [V/m]
E_{in}	input field amplitude [V/m]
E_{out}	output field amplitude [V/m]
$\overline{E}_{tube}$	ray tube electric field strength [V/m]
f_{sub}	subreflector focal length [m]
F_{holo}	focal point of a hologram [m]
$\overline{H}$	magnetic field strength [A/m]
$\overline{H}_0$	0^{th} order term of magnetic field strength [A/m]
$\overline{H}_i$	i^{th} order term of magnetic field strength [A/m]
i	index
j	imaginary unit

$\overline{J}_s$	electric surface current [A/m]
k	wave number [1/m]
$\overline{k}$	wave vector [1/m]
k_0	wave number in free-space [1/m]
l	ray length [m]
L	eikonal function [m], extension length [m]
m	ray number index
M	number of rays
$\overline{M}_s$	magnetic surface current [V/m]
n	index of refraction, ray number index
n_{tube}	ray tube index
$\overline{n}$	surface normal unit vector
N	number of rays, degree of a function
P	power [W]
P_{diel}	dielectric loss [W]
P_{in}	input power [W]
P_{out}	output power [W]
P_{refl}	reflected power [W]
P_{spill}	spillover power [W]
P_{tot}	total power [W]
$\overline{r}$	position vector [m]
r_{main}	main reflector distance from the output aperture [m]
r_{sub}	distance between reflectors [m]
R	radius [m]
s	distance along a ray [m]
$\overline{s}$	ray direction unit vector
$\overline{s}_0$	ray starting point [m]
$\overline{s}_1^{\parallel}$	incident ray direction unit vector
$\overline{s}_1^{\prime\parallel}$	reflected ray direction unit vector
$\overline{s}_2^{\prime\parallel}$	refracted ray direction unit vector
$\overline{s}_r$	ray vector [m]
S	surface
t	time [s]
$\tan\delta$	loss tangent
$\overline{u}_1^{\parallel}$	parallel polarisation of incident electric field unit vector
$\overline{u}_1^{\prime\parallel}$	parallel polarisation of reflected electric field unit vector
$\overline{u}_2^{\prime\parallel}$	parallel polarisation of refracted electric field unit vector
$\overline{u}_1^{\perp}$	perpendicular polarisation of incident electric field unit vector

$\overline{u}_1'^{\perp}$	perpendicular polarisation of reflected electric field unit vector
$\overline{u}_2'^{\perp}$	perpendicular polarisation of refracted electric field unit vector
α_{feed}	subreflector offset angle
α_{sub}	main reflector offset angle
ε	permittivity [As/Vm]
ε_0	permittivity in free-space [As/Vm]
ε_r	relative permittivity
η	wave impedance [Ω]
θ_1	incident angle
θ_1'	reflection angle
θ_2	refraction angle
θ_{feed}	feed horn half-beam width
θ_{main}	output half-beam width
μ	permeability [Vs/Am]
μ_0	permeability in free-space [Vs/Am]
μ_r	relative permeability
ρ	input field aperture cylindrical coordinate [m]
ρ'	output field aperture cylindrical coordinate [m]
$\rho_{\parallel}$	parallel polarisation reflection coefficient
$\rho_{\perp}$	perpendicular polarisation reflection coefficient
ρ_c	half-power point of a Butterworth function [m]
$\tau_{\parallel}$	parallel polarisation transmission coefficient
$\tau_{\perp}$	perpendicular polarisation transmission coefficient
ϕ	input field aperture cylindrical coordinate
Φ	phase
Φ_{in}	input field phase pattern
Φ_{out}	output field phase pattern
ω	angular frequency [rad/s]

List of abbreviations

APC	antenna pattern comparison technique
AUT	antenna under test
CATR	compact antenna test range
DRFS	dual reflector feed system
FDTD	finite-difference time-domain
GO	geometrical optics
HFSS	high frequency structural simulator
ILA	integrated lens antenna
LTCC	low-temperature co-fired ceramic
MoM	method of moments
PEC	perfect electric conductor
PO	physical optics
PTD	physical theory of diffraction
QZ	quiet-zone
RTO	representative test object
TE	transverse electric
TM	transverse magnetic

1. Introduction

1.1 Background

The millimetre and submillimetre wave frequency ranges (30 GHz – 3 THz) have many current and potential applications. Several scientific satellites have been launched into space with large reflector antennas equipped with millimetre and submillimetre wave receivers. For example, Planck satellite was launched in 2009 and it is used to map the cosmic microwave background radiation and its foregrounds at several frequency bands from 30 GHz up to 857 GHz [1]. In order to ensure that the expensive and complicated satellite antenna systems operate correctly, the antenna radiation characteristics need to be measured prior to launch. At higher frequencies, in antenna measurement as well as in antenna manufacturing, mechanical accuracy requirements become very demanding.

Large atmospheric attenuation largely prevents the use of submillimetre waves over long distances in ground based applications. On the other hand, at millimetre wave frequencies, e.g., high speed data links are feasible. At E-band (71 GHz – 86 GHz) bandwidths of several gigahertz are licensed for telecommunication applications [2]. Also, e.g., automotive radar at 77 GHz – 81 GHz requires beam-steering antenna with a narrow high-directivity beam [3].

Electrically large antennas are needed in many applications, e.g., in order to achieve high antenna gain with a narrow beam. Reflector and lens antennas, with all dimensions large compared to the wavelength, are commonly designed using ray tracing. Ray tracing is based on geometrical optics (GO) that is a high frequency approximation of Maxwell's equations, i.e., all dimensions are assumed to be large compared to the wavelength. The main advantage of ray tracing is the decreased computational effort

as compared to more accurate full-wave methods.

1.2 Motivation and scope of the thesis

In this thesis, ray tracing is used in both synthesis and simulation of electrically large antennas. In antenna synthesis the shape of the antenna is calculated from the known and desired field distributions. In antenna simulation the electrical properties of the known antenna are calculated. The synthesis and simulation methods are used to design several different antennas. An important task of any antenna design work is to test the designed antenna with measurements, and therefore antenna measurements are used in this thesis to verify the simulation results.

A 650 GHz dual reflector feed system (DRFS) is designed with a synthesis method based on ray tracing. The DRFS is used in a hologram-based compact antenna test range (CATR) to test a 1.5-m diameter antenna. Using a modified illumination, provided with the DRFS, the operation of the hologram is improved as the required amplitude tapering is included in the illumination and narrow slots can be avoided in the hologram pattern.

In this thesis, several beam-steering integrated lens antennas (ILAs) for E-band are designed with ray-tracing simulations and tested with radiation pattern measurements. In an ILA, a planar feed array, together with a switching network, is integrated into direct contact with the dielectric lens. Beam steering is achieved by switching between the feed elements. This work aims at improvement of the beam-steering properties by optimising the shape of the lens for improved performance for large beam-steering angles. A typical disadvantage of a beam-steering ILA is the increasing internal reflections with feed elements away from the focal point of the lens. The last part of this thesis focuses on designing lens shapes with reduced levels of internal reflections. Also, beam-steering properties of ILAs with a wide range of different lens permittivities and feed element directivities are studied with the conventional and with the proposed lens designs.

The ray tracing synthesis and simulation methods are introduced in Chapter 2. Chapter 3 concentrates on designing and testing of the 650 GHz DRFS and its use in a hologram-based CATR. Chapter 4 presents the ILA designs and test results. Summary of the articles and conclusions are in Chapter 5 and Chapter 6, respectively.

1.3 Scientific contributions of the thesis

The scientific contributions of the thesis are:

1. Design and testing of a 650 GHz dual reflector feed system producing the desired modified beam shape. Increased understanding and improvement of the used synthesis method in antenna design. [I,II]

2. Antenna measurements and analysis of results of a 1.5-m diameter antenna at 650 GHz in a hologram-based antenna test range. So far, this is the highest frequency at which any CATR has been used for antenna tests. [III]

3. Comparison of beam-steering integrated lens antennas with different lens permittivities and feed element directivities. [IV,VI,VIII,IX,XI]

4. Design and measurement of two beam-steering integrated lens antennas at 77 GHz with feed arrays and switching networks integrated in low-temperature co-fired ceramic (LTCC). The lenses together with the feed arrays and switching networks enable electronic beam steering. [V,VII]

5. The optimal eccentricity of a low permittivity integrated lens for a high-gain beam-steering antenna is found. A prototype is tested and analysed at 77 GHz. [VI,VII]

6. Extended hemispherical integrated lens antenna with feeds on a spherical surface is found to have very low scan loss. A prototype is tested and analysed at 77 GHz. [IX]

7. A method to reduce internal reflections in low permittivity extended hemispherical integrated lens antennas is developed. A prototype is tested and analysed at 77 GHz. [VIII,IX]

8. A method to reduce internal reflections in integrated lens antennas with any lens permittivity or feed element directivity is developed. [X,XI]

2. Ray tracing in antenna design

Ray tracing is used to calculate paths of many different kinds of waves. Ray tracing is used, e.g., in acoustics to calculate sound waves and in seismology to calculate seismic waves. The most traditional use of ray tracing is in optics in, e.g., designing optical lenses and other optical systems. Ray tracing is also used in computer graphics for image generation. Furthermore, ray tracing is used to calculate propagation of radio signals and in propagation channel prediction.

In this thesis, ray tracing based on geometrical optics (GO) is used in antenna design. Theory of GO is briefly introduced in Section 2.1 and ray tracing in isotropic homogeneous media in Section 2.2. Ray-tracing antenna design techniques are divided into two subsections. Antenna synthesis techniques using ray tracing are reviewed in Section 2.3 and ray-tracing simulations are reviewed in Section 2.4. The dual reflector antenna synthesis method used in this thesis is introduced in more detail in Section 3.3. The integrated lens antenna simulations with ray tracing are introduced in Section 4.1.

2.1 Geometrical optics

Geometrical or ray optics is widely used in the design of electrically large lens and reflector antennas. GO is a high frequency approximation of Maxwell's equations [4–6]. The high frequency approximation is accurate if all distances, radii of curvature, etc., are large compared to the wavelength. In principle, GO assumes that effects due to diffraction are negligible. With optical systems the dimensions are typically very large compared to the wavelength and the geometrical optics approximation is accurate [4]. At radio frequencies the dimensions can be from several up to a few tens of wavelengths and therefore the accuracy of GO may be

compromised. Nevertheless, GO can provide meaningful and useful approximative results.

The geometrical optics approximation is derived from the electric and magnetic field expansions as power series of inverse powers of the angular frequency [4]

$$\overline{E}(\omega,\overline{r}) = e^{-jk_0L(\overline{r})}\sum_{i=0}^{\infty}\frac{\overline{E}_i(\overline{r})}{(j\omega)^i} \tag{2.1}$$

$$\overline{H}(\omega,\overline{r}) = e^{-jk_0L(\overline{r})}\sum_{i=0}^{\infty}\frac{\overline{H}_i(\overline{r})}{(j\omega)^i}, \tag{2.2}$$

where $L(\overline{r})$ is the so-called eikonal function and $k_0 = \omega\sqrt{(\mu_0\varepsilon_0)}$. Time dependence of $e^{-j\omega t}$ is assumed. At high frequencies the 0^{th} order term dominates. The 0^{th} order equations describe the geometrical optics field.

The geometrical optics field vectors $\overline{E}_0$, $\overline{H}_0$, and $\overline{k}(\overline{r}) = k_0\nabla L(\overline{r})$ are perpendicular to each other. The surface where the phase is constant is given by the surface where Re$\{L\}$ is constant. When L is real, power propagates in the direction of $\overline{k}$, i.e., perpendicular to the constant phase front (L is complex in lossy material and in the shadow region [5]). The phase Φ on a general phase front is [4]

$$\Phi(\overline{r}) = \omega t - \frac{\omega}{c_0}L(\overline{r}), \tag{2.3}$$

where c_0 is the speed of light in free space.

The eikonal function determines the ray directions and the wave fronts. The eikonal function is determined from the so the called eikonal equation [4]

$$|\nabla L(\overline{r})| = \sqrt{\mu_r(\overline{r})\varepsilon_r(\overline{r})} = n(\overline{r}), \tag{2.4}$$

where $n(\overline{r}) = \sqrt{\mu_r(\overline{r})\varepsilon_r(\overline{r})}$ is the index of refraction of the medium. Differential equations for determining ray paths and fields can be derived from the eikonal equation [4]. For example, in homogeneous medium n is constant and the eikonal function is [4]

$$L(s) = ns + L(s_0), \tag{2.5}$$

where s is a distance along a ray. The geometrical optics approximation is a local plane wave propagating along a ray

$$\overline{E}_0 = \eta\overline{H}_0 \times \overline{s} \tag{2.6}$$

$$\overline{H}_0 = \frac{1}{\eta}\overline{s} \times \overline{E}_0, \tag{2.7}$$

where $\eta = \sqrt{\varepsilon/\mu}$ is the wave impedance and $\overline{s}$ is the ray direction unit vector. The ray direction is perpendicular to the wave front and can be

calculated from the eikonal function [4]

$$\overline{s} = \frac{\nabla L}{n}. \tag{2.8}$$

In geometrical optics the concept of rays is useful in understanding and illustrating the propagation of geometrical optics fields. A ray is a line in space that represents the direction of propagation. The ray path and field along the ray can be calculated. Rays that pass through a given closed curve constitute a ray tube [4].

Ray tubes are useful in understanding and calculating propagation of power. In general, rays and ray tubes are used as conceptual aid in deriving equations or functions that describe analytical solution to the given problem. Usually, in the implementation of geometrical optics, the properties of single rays are not calculated.

2.2 Ray tracing

In ray tracing fields are calculated by determining the path of a finite number of rays. First, rays are calculated from a known field, and then these rays are traced one by one (their path is calculated) through materials, reflections, refractions, etc., and finally the desired field is calculated from the resulting ray distributions, ray lengths, etc. Complex systems can be analysed as it is not necessary to derive an analytical solution.

Properties of geometrical optics fields and rays are described in Sections 2.2.1 and 2.2.2 in homogeneous, isotropic, and low loss medium. Wave fronts and material surfaces are approximated with planes and the field in a ray tube is calculated from the average of the ray amplitudes. The source is approximated as a single point source, i.e., no extended sources are used [6, 7]. These approximations are used in the ray-tracing synthesis method in Chapter 3 and in the ray-tracing simulations in Chapter 4. With these approximations the geometrical optics equations are greatly simplified. Similar ray tube tracing method is used, e.g., in [8, 9].

In general, there are several different levels of local approximation in representing fields with rays. Often the wave front is approximated with a second-order approximation that is characterised with two principal radii and directions of curvature, e.g., in [4–6, 10, 11].

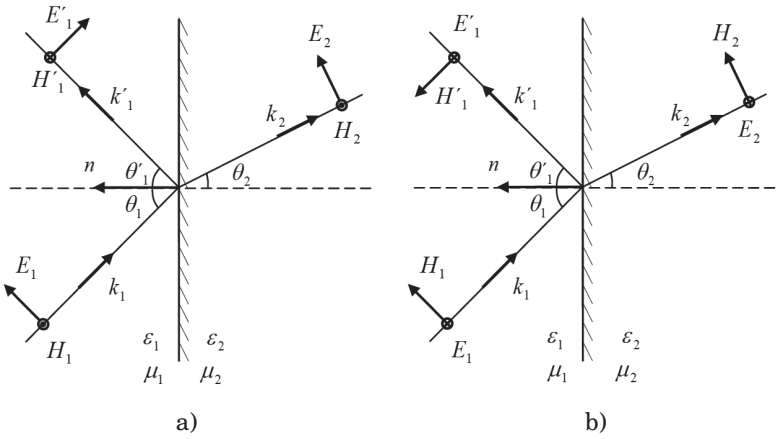

Figure 2.1. Reflection and refraction of a plane wave at a planar interface of two lossless media: a) parallel polarisation, and b) perpendicular polarisation.

2.2.1 Ray path

A ray in a homogeneous medium is a straight line. For homogeneous medium ($n(\overline{r}) = n$), a ray can be described simply as

$$\overline{s}_r = \overline{s}_0 + s\overline{s}, \tag{2.9}$$

where s is the distance along a ray, $\overline{s}$ is the ray direction unit vector, and $\overline{s}_0$ is the starting point of the ray. The ray direction approximates the direction of propagation, i.e., the ray direction is the same as that of the local wave vector $\overline{k} = k\overline{s}$.

When a ray (a plane-wave) encounters a boundary between two different media, it is reflected and refracted from the boundary, as illustrated in Figure 2.1. The incident wave comes at an angle θ_1 compared to the surface normal unit vector $\overline{n}$. A part of the incident wave is reflected at an angle θ_1' and a part is refracted (transmitted) into medium 2 at an angle θ_2. The geometrical optics approximation is locally a plane wave and the material surface is approximated as the tangential surface at the point of incidence. Let us assume in the following that the materials are lossless and $\mu_1 = \mu_2 = \mu_0$. In general, these are good approximations in case of the reflectors and dielectric lenses.

The angle of incidence and the angle of reflection are equal, $\theta_1 = \theta_1'$, and the refraction angle is calculated from Snell's law

$$n_1 \sin\theta_1 = n_2 \sin\theta_2, \tag{2.10}$$

where $n_1 = \sqrt{\varepsilon_{r1}}$ and $n_2 = \sqrt{\varepsilon_{r2}}$. Reflected $\overline{s}_1'$ and refracted $\overline{s}_2$ ray direc-

tions are calculated using Snell's law and from the surface normal vector $\overline{n}$. The ray directional vectors $\overline{s}_1$, $\overline{s}'_1$, $\overline{s}_2$, and the surface normal vector $\overline{n}$ lay on the same plane.

Next, the field on both sides of the boundary are solved. Because the field along the ray is the local plane wave approximation of (2.6) and (2.7), it is sufficient to solve only the electric or magnetic field. The electric field vectors of the reflected and refracted (transmitted) rays are calculated first by dividing the known incident field $\overline{E}_1$ to the parallel $E_1^{\parallel}\overline{u}_1^{\parallel}$ and perpendicular $E_1^{\perp}\overline{u}_1^{\perp}$ components

$$\overline{E}_1 = E_1^{\parallel}\overline{u}_1^{\parallel} + E_1^{\perp}\overline{u}_1^{\perp}, \tag{2.11}$$

where

$$E_1^{\perp} = \overline{E}_1 \cdot \overline{u}_1^{\perp} \quad , \quad E_1^{\parallel} = \overline{E}_1 \cdot \overline{u}_1^{\parallel}\,, \tag{2.12}$$

where $\overline{u}_1^{\perp}$ and $\overline{u}_1^{\parallel}$ are the perpendicular (transverse electric- or TE- polarisation) and parallel polarisation (transverse magnetic- or TM- polarisation) unit vectors, respectively. These polarisation direction unit vectors are calculated from incident ray direction $\overline{s}_1$ and from the surface normal $\overline{n}$

$$\overline{u}_1^{\perp} = \frac{\overline{n} \times \overline{s}_1}{|\overline{n} \times \overline{s}_1|} \quad , \quad \overline{u}_1^{\parallel} = \frac{\overline{s}_1 \times \overline{u}_1^{\perp}}{|\overline{s}_1 \times \overline{u}_1^{\perp}|}\,. \tag{2.13}$$

Fresnel reflection and transmission coefficients for parallel and perpendicular polarisations are calculated from the incident angle θ_1 and from the relative permittivities of the two medium

$$\rho_{\parallel} = \frac{E_1'^{\parallel}}{E_1^{\parallel}} = \frac{\sqrt{\frac{\varepsilon_{r2}}{\varepsilon_{r1}} - \sin^2\theta_1} - \frac{\varepsilon_{r2}}{\varepsilon_{r1}}\cos\theta_1}{\sqrt{\frac{\varepsilon_{r2}}{\varepsilon_{r1}} - \sin^2\theta_1} + \frac{\varepsilon_{r2}}{\varepsilon_{r1}}\cos\theta_1} \tag{2.14}$$

$$\tau_{\parallel} = \frac{E_2^{\parallel}}{E_1^{\parallel}} = \frac{2\sqrt{\frac{\varepsilon_{r2}}{\varepsilon_{r1}}}\cos\theta_1}{\sqrt{\frac{\varepsilon_{r2}}{\varepsilon_{r1}} - \sin^2\theta_1} + \frac{\varepsilon_{r2}}{\varepsilon_{r1}}\cos\theta_1} \tag{2.15}$$

$$\rho_{\perp} = \frac{E_1'^{\perp}}{E_1^{\perp}} = \frac{\cos\theta_1 - \sqrt{\frac{\varepsilon_{r2}}{\varepsilon_{r1}} - \sin^2\theta_1}}{\sqrt{\frac{\varepsilon_{r2}}{\varepsilon_{r1}} - \sin^2\theta_1} + \cos\theta_1} \tag{2.16}$$

$$\tau_{\perp} = \frac{E_2^{\perp}}{E_1^{\perp}} = \frac{2\cos\theta_1}{\sqrt{\frac{\varepsilon_{r2}}{\varepsilon_{r1}} - \sin^2\theta_1} + \cos\theta_1}\,. \tag{2.17}$$

The reflected and refracted (transmitted) fields are

$$\overline{E}'_1 = \rho_{\parallel}E_1^{\parallel}\overline{u}_1'^{\parallel} + \rho_{\perp}E_1^{\perp}\overline{u}_1'^{\perp} \tag{2.18}$$

$$\overline{E}_2 = \tau_{\parallel}E_1^{\parallel}\overline{u}_2^{\parallel} + \tau_{\perp}E_1^{\perp}\overline{u}_2^{\perp}\,, \tag{2.19}$$

where

$$\overline{u}_1'^{\perp} = \frac{\overline{n} \times \overline{s}'_1}{|\overline{n} \times \overline{s}'_1|} \quad , \quad \overline{u}_1'^{\parallel} = -\frac{\overline{s}'_1 \times \overline{u}_1'^{\perp}}{|\overline{s}'_1 \times \overline{u}_1'^{\perp}|} \tag{2.20}$$

$$\overline{u}_2^{\perp} = \frac{\overline{n} \times \overline{s}_2}{|\overline{n} \times \overline{s}_2|} \quad , \quad \overline{u}_2^{\parallel} = \frac{\overline{s}_2 \times \overline{u}_2^{\perp}}{|\overline{s}_2 \times \overline{u}_2^{\perp}|} \, . \tag{2.21}$$

If $\varepsilon_{r1} > \varepsilon_{r2}$, a total reflection occurs if:

$$\theta_1 \geq \sin^{-1}(\sqrt{\frac{\varepsilon_{r2}}{\varepsilon_{r1}}}). \tag{2.22}$$

In case of a total reflection, reflection coefficients become complex numbers and $|\rho_{\perp}| = |\rho_{\parallel}| = 1$, i.e., all incoming power is reflected. Reflection coefficients are calculated from (2.14) and (2.16) and they affect only the phase of the reflected ray. The phase change depends on polarisation and angle of incidence.

In general, metal reflector surfaces can be considered as perfect electric conductor (PEC) surfaces. The reflection coefficient from a PEC surface for all polarisations and for all incident angles is $\rho_{\perp} = \rho_{\parallel} = -1$.

2.2.2 Fields and power

In general, in ray-tracing calculations of reflector or lens antennas, it is common to approximate that the feed antenna is a point source. The original field values for the rays can be determined from a known far-field pattern of the feed that is defined as an angular field distribution originating from the focal point, from where all the rays also originate.

As a single ray is traced, with the first order approximation of the wave front, only the phase of the field changes along the ray in lossless medium. When lossy dielectrics are considered also the amplitude changes. Field along a single ray does not represent the geometrical optics approximation of the field because a single ray does not include divergence or convergence of the wave front. The fields calculated in Section 2.2.1 describe how the field along a single ray changes on the boundaries of different materials.

The wave front properties are calculated with ray tubes defined by several rays. Power and the fields are calculated for ray tubes intersecting a surface. A ray tube is illustrated in Figure 2.2. The smallest number of rays that can define a ray tube is three. It is more common to use ray grids defined in polar coordinates and four rays per ray tube as, e.g., in [12].

The original field values for the rays are determined directly from the far-field pattern of the feed

$$\overline{E} = \overline{E}_{feed}(\theta, \phi), \tag{2.23}$$

where $\overline{E}$ is the field value for the ray at the surface, at which the ray-tracing fields are originally calculated, in direction (θ, ϕ) in the local coordinate system of the feed whose origin is at the focal point of the feed.

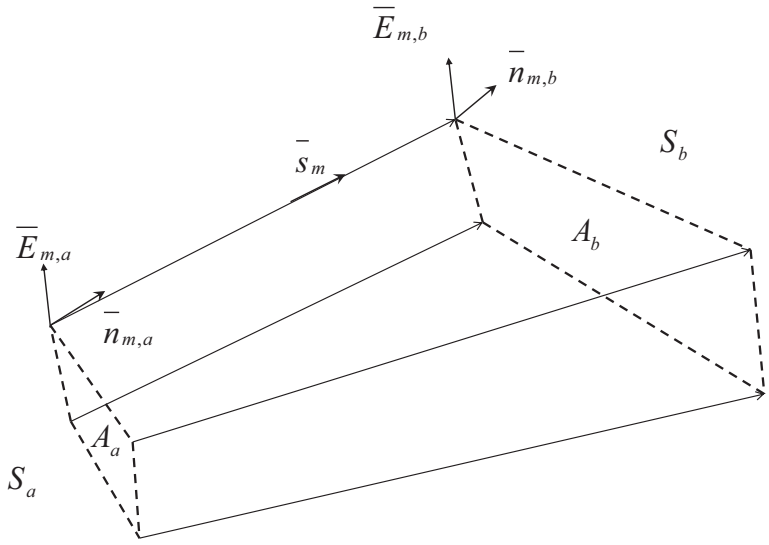

Figure 2.2. Example of a ray tube from surface S_a to S_b. A ray tube between two surfaces is fully defined with the parameters of the material between the surfaces and with the ray intersection points, ray amplitudes, and surface normal vectors at the ray intersection points on the surfaces.

Ray-tracing is calculated from surface to surface. An example of a ray tube from surface S_a to S_b is illustrated in Figure 2.2. In the following, the calculation of the field and power from S_a to S_b is explained.

Electric field changes along m^{th} ray from S_a to S_b

$$\overline{E}_{m,b} = \overline{E}_{m,a} e^{-jk(s_{m,b}-s_{m,a})} e^{-\frac{1}{2}\tan\delta \cdot k(s_{m,b}-s_{m,a})}, \tag{2.24}$$

where $\overline{E}_{m,b}$ and $\overline{E}_{m,a}$ are the fields along the ray at the intersection points of the ray at surfaces S_a and S_b, respectively, and $s_{m,b}-s_{m,a}$ is the length of the ray between the surfaces, and $\tan\delta$ is the loss tangent of the medium. The first exponent term in (2.24) includes the phase change along the ray. The second exponent term in (2.24) includes an approximation of dielectric loss in case of low-loss material [13], i.e.,

$$Im\{k\} \approx \frac{1}{2}\tan\delta \cdot k, \tag{2.25}$$

with $tan\delta = Im\{\varepsilon_r\}/Re\{\varepsilon_r\} \ll 1$.

The power and field of a ray tube on the surfaces are calculated next. In general, the ray tube may intersect the surface at an angle. The tube cross-section is defined as a surface that is perpendicular to the rays. The

cross-sectional areas are approximated as

$$A_{cross,a} \approx A_a(\frac{1}{M}\sum_{m=1}^{M}\overline{s}_m \cdot \frac{1}{M}\sum_{m=1}^{M}\overline{n}_{m,a}) \tag{2.26}$$

$$A_{cross,b} \approx A_b(\frac{1}{M}\sum_{m=1}^{M}\overline{s}_m \cdot \frac{1}{M}\sum_{m=1}^{M}\overline{n}_{m,b}), \tag{2.27}$$

where A_a and A_b are the areas on the surfaces that the ray-tube intersects, and M is the number of rays that define the ray tube, $\overline{s}_m$ is the ray direction of the m^{th} ray, and $\overline{n}_{m,a}$ and $\overline{n}_{m,b}$ are the unit normal vectors on the surfaces at the intersection points of the ray.

The electric field of the local plane wave approximation on the surface S_b intersected by the ray tube is

$$\overline{E}_{tube,b} \approx \frac{1}{M}\sum_{m=1}^{M}\overline{E}_{m,b}\sqrt{\frac{A_{cross,a}}{A_{cross,b}}}, \tag{2.28}$$

where $\overline{E}_{m,b}$ are the ray fields from (2.24). If needed, the magnetic field can be calculated with (2.7). In general, it can be said that $\overline{E}_{tube,b}$ is the geometrical optics approximation field on the surface area $A_{cross,b}$. If a single coordinate point needs to be defined for the field value, it can be considered to lie at the centre point of A_b.

Power that propagates through the surface S_b in a ray tube is calculated from the real part of Poynting's vector

$$P = \frac{1}{2}Re\{\int_S \overline{E} \times \overline{H}^* \cdot \overline{dS}\}. \tag{2.29}$$

Power inside a ray tube on the surface S_b is then approximated as

$$P_{tube,b} \approx \frac{1}{2\eta}|\overline{E}_{tube,b}|^2 A_{cross,b}. \tag{2.30}$$

In lossless material ($\tan\delta = 0$) power does not change, i.e., $P_{tube,a} = P_{tube,b}$. The total power passing through a surface is simply the sum of the powers in all of the ray tubes intersecting the surface.

On the interface between two materials the field and power components of the incident, reflected, and refracted ray-tubes can be calculated similarly with the fields along the rays ((2.11), (2.18), and (2.19)) and with cross-sectional areas of the incident, reflected, and refracted ray-tubes.

2.3 Ray-tracing antenna synthesis

Antenna synthesis means that the reflector or lens surfaces are calculated, i.e., synthesised, by some means from a known feed radiation and

desired radiation of the antenna. Synthesis methods can be divided into different groups in many ways. The synthesis methods can be divided into direct and indirect methods. In indirect methods the aperture field of the antenna is calculated from the desired far-field and the shaped surfaces are synthesised to produce that aperture field. The direct methods use the desired far-field in the synthesis. The synthesis methods can also be divided based on the method used to calculate the electromagnetic fields. Most synthesis methods are based on geometrical optics or physical optics. Physical optics methods are sometimes called diffraction synthesis methods, because diffracted fields are often included by using physical theory of diffraction (PTD).

Synthesis methods are usually developed for a specific antenna type. Synthesis methods can be divided to reflector synthesis methods and lens synthesis methods. Some synthesis methods can be used for both reflector and lens antennas. Usually a synthesis method is used with some kind of optimisation, where the synthesis objective (or basic geometry etc.) is changed, the shaped surfaces are synthesised, and then the antenna is analysed and compared with the design objective.

Examples of GO and ray-tracing reflector and lens antenna synthesis methods are described in the following paragraphs.

A GO-based indirect synthesis method is presented in [14]. The shaped dual reflector surfaces are determined by solving a pair of first-order ordinary non-linear differential equations. An example of a dual-reflector system, which will produce a uniform phase and amplitude distribution in the aperture of the reflector, is given. Another example of a GO-based indirect synthesis method based on solving a non-linear second-order partial differential equation is given in [15]. The Monge-Ampère type equation is solved numerically by using an iterative procedure that converges to the actual solution [15]. A direct GO-based method for axis-symmetric substrate lens is presented in [16]. GO is used to obtain the first guess of the lens shape and physical optics (PO) formulation is used to compute the actual far-field radiation pattern. In [17], the method is generalised also for a shaped double-shell dielectric lens antenna. An indirect GO-based dielectric lens synthesis method is presented in [18]. The profiles of rotationally symmetric lens surfaces are calculated numerically from a non-linear differential equation.

An indirect ray-tracing based synthesis method is presented in [19]. It is formulated for a shaped dual offset reflector antenna based on a ba-

sic geometry of either a Cassegrain or a Gregorian system. Rotational symmetry is assumed for feed pattern and for the desired aperture field pattern. A first-order approximation is used for the surfaces. A similar method is used in [20] to design a dielectric bifocal lens, where the shape of the two lens surfaces are synthesised for focusing from the two focal points.

Reflector surfaces and wave fronts are described in terms of curvature parameters of the bi-parabolic expansions in [10]. It is an indirect ray-tracing based synthesis method for dual offset reflector antennas. To get the aperture mapping exact, extra variables are added to the mapping, i.e., by allowing the radial lines of the aperture ray grid to be curved. Using the bi-parabolic expansions for surfaces and wave-fronts makes the solution easier to control [10]. The synthesis technique has been used for shaped offset dual reflectors antennas and for a dual reflector feed for a spherical reflector.

In [21], a ray-tracing based synthesis method, with a first-order approximation for the surfaces, i.e., tangential planes, is presented. The method is used to design a dual reflector feed system (DRFS) for a single offset reflector CATR. The surfaces are extrapolated based on a tangential plane at the previous point. Another indirect ray tracing based synthesis method, with the first-order approximation for the surfaces, is presented in [22]. A dielectric lens synthesis method based on indirect ray-tracing is presented in [23]. A first-order approximation is used for the surfaces of the rotationally symmetric lens. The lens has two shaped surfaces, similarly as dual reflector antennas, allowing the control of both amplitude and phase of the aperture field.

A direct ray-tracing synthesis method for designing a feed system for a hologram-based CATR is described in [12, 24, 25]. The synthesis method was developed specifically for designing a DRFS for a hologram-based CATR. This synthesis method is used in this thesis in designing a 650 GHz dual reflector feed system (Chapter 3 and [I–III]). In this method, the first-order approximation is used for the local approximation of the reflector surfaces and for the wave fronts.

2.4 Ray-tracing antenna simulation

Large reflector and lens antennas are commonly simulated using ray tracing. The main advantage of ray tracing is the decreased computational

effort compared to more accurate full-wave methods.

Ray tracing is usually used in combination with other simulation methods. Rays are launched from the source, traced through reflections and/or refractions, and the resulting field is calculated on a surface. The most typical example is a reflector (or lens) antenna, where the rays are launched from the focal point of a feed antenna, simulated (or measured) radiation pattern of the feed is used to calculate the initial fields for the rays, and the result of the ray-tracing simulation is the aperture field and the far-field is solved from the aperture field using Huygens' method, i.e., aperture integration of equivalent surface currents.

Typically the feed radiation pattern is calculated with some other simulation method or simulation software, e.g., method of moments (MoM) [26], HFSS [27], or by assuming theoretical current distribution for the feed [28, 29]. It is also possible to use some simple function to model the feed radiation pattern, e.g., [11, 30, 31], or a measured feed radiation pattern as in [32]. The source that gives the initial field can be a plane wave, if the antenna is simulated in a receiving mode [33].

Typically in ray-tracing antenna simulations the wave front along a ray is approximated with a second-order approximation that is characterised with two principal radii and directions of curvature, e.g., in [4, 6, 11, 26, 28, 30]. With the second-order approximation, the field is calculated and traced along each ray. The first-order approximation ray represents a plane wave and the wave front divergence or convergence is calculated from the changing cross-sectional area of the ray tube. With the first-order approximation, the field is calculated and traced along each ray tube. This approximation is used in this thesis, and also, e.g., in [8, 9].

In principle, the rays can be traced to the far-field. However, especially with directive antennas, ray-tracing does not predict the far-field accurately, therefore ray-tracing is used to calculate the aperture field. The far-field is solved using Love's field equivalence principle for the region outside the antenna, i.e., a precise expression and a generalisation of Huygens' principle [34]. The equivalent electric and magnetic currents are calculated from the tangential components of magnetic and electric fields, respectively, at the aperture surface and the far-field is integrated from the equivalent currents. Aperture surface is chosen as a surface near or on the antenna, on which it is convenient to make assumptions regarding the field values for the purpose of computing fields at external points [35].

In this thesis, ray-tracing simulations are used in designing several

beam-steering integrated lens antennas (ILAs) in Chapter 4 and in [IV–XI].

3. Dual reflector feed system (DRFS)

Development of a hologram-based compact antenna test range (CATR) started in the 1990's [36, 37]. Since then antenna tests have been conducted at 39 GHz [38], 119 GHz [39], 322 GHz [40, 41], and 650 GHz [III].

A dual reflector feed system (DRFS) can be used to provide shaped illumination that simplifies the hologram manufacturing [12, 42]. The hologram-based CATR and the use of a DRFS in it are introduced in Sections 3.1 and 3.2, respectively. The DRFS is designed using a ray-tracing based synthesis method [12,24,25,42]. The synthesis method is described in Section 3.3.

A 650 GHz DRFS was designed [I] and tested [II] as a part of an antenna measurement campaign aiming at the measurement of a 1.5-m diameter antenna at 650 GHz [III]. The design and testing of the 650 GHz DRFS are described in Sections 3.4 and 3.5, respectively, and the antenna tests in a CATR at 650 GHz in Section 3.6.

3.1 Hologram-based CATR

A hologram-based compact antenna test range is using a computer generated radio-wave hologram instead of a more common reflector or a set of reflectors, e.g., [21,43–45], or a lens [43,46,47]. A hologram is an interference pattern of the wave-front illuminating the hologram and the desired goal field. In a CATR, the goal field is a plane wave in the quiet zone. The hologram is illuminated with a spherical wave from a feed horn [38–41] or from a DRFS [42], [III]. The computer generated hologram design is explained in detail in [48,49], and the design of a hologram for a hologram-based CATR in [36, 37, 50–52].

There are four different hologram types that can be used in a CATR; a transmission-type amplitude hologram [36–41], a transmission-type phase

Figure 3.1. Example of a transmission-type amplitude hologram pattern. Metal is in black and slots in white. [III]

hologram [53–56], a reflection-type amplitude hologram [57], or a reflection-type phase hologram [58, 59].

All the holograms used in the reported antenna tests have been transmission-type amplitude holograms. An example of a hologram pattern is presented in Figure 3.1. The pattern consists of vertical, slightly curved slots on a metal plated dielectric film. It is called an amplitude hologram, because it modulates the field by blocking the field at the metal strips and by transmitting through the slots. A schematic layout of a typical hologram-based CATR using a transmission-type amplitude hologram is shown in Figure 3.2. The quiet-zone (QZ) field is produced at an angle of 33° in order to avoid direct radiation through the hologram to the QZ. The antenna under test (AUT) is placed in the QZ and rotated in the antenna tests.

In principle, in the transmission-type amplitude holograms, the width of a slot corresponds to an amplitude modification and the position of the slot corresponds to a phase modification. The hologram pattern is optimised based on two-dimensional simulations [37, 50]. The quiet-zone field is calculated with physical optics (PO) from the aperture field. Because the whole hologram is too large to simulate in one simulation, only one cut of the nonuniform metal grating is analysed at once. Also the PO calculation is done in only two dimensions, i.e. in the same plane as the FDTD simulation [37]. The cross-polarisation can not be analysed in the two-dimensional simulations, therefore the cross-polarisation is calculated with a method presented in [51].

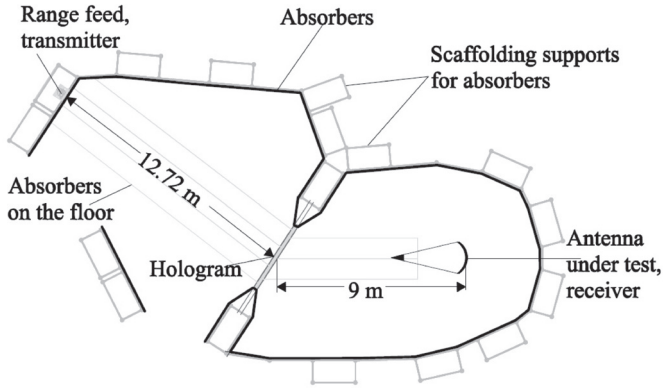

Figure 3.2. Layout of a CATR based on a transmission-type hologram. [III]

The advantages of a hologram-based CATR for testing large antennas at high frequencies are relatively low surface accuracy requirement, low cost, and ease of fabrication. Surface accuracy requirement of a reflector is approximately $\lambda/100$ [60]. As the hologram is a transmission type element, the planarity requirement is much less demanding [61]. The required hologram pattern accuracy of $\lambda/100$–$\lambda/50$ [62, 63] is easier to achieve with the planar hologram than a similar accuracy for a three dimensional reflector. A hologram is a light weight structure making it possible to transport the hologram to the AUT, if transporting the large antenna is not possible. In the conducted antenna measurement campaigns, the CATR has been constructed and antenna tests have been done in a relatively short time [38–41], [III]. The main disadvantage is a relatively narrow bandwidth of $\pm 10\%$ [62].

Also other measurement techniques have been used to test sizable antennas at submillimeter wavelengths, e.g., a reflector based CATR up to 500 GHz [64, 65]. The main disadvantage compared to a hologram-based CATR is the need of very large high precicion reflectors. Near-field measurements have been reported up to about 650 GHz [66, 67]. The disadvantage of near-field measurements is the need of a high precision scanner and very stable measurement equipment due to long measurement time needed.

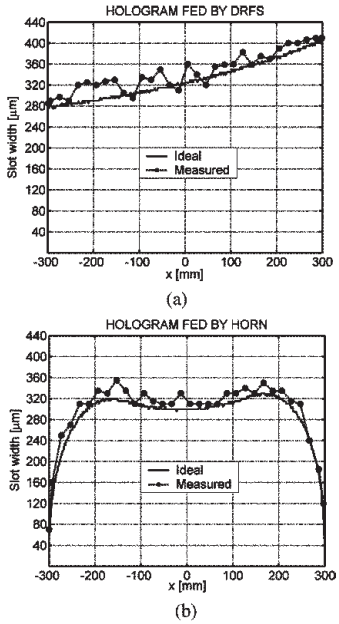

Figure 3.3. Example of slot widths in the 310 GHz holograms (a) with a modified illumination and (b) with a direct illumination with a feed horn. [42]

3.2 Feed system for a hologram based CATR

Traditionally, a corrugated feed horn has been used to illuminate the hologram with a Gaussian spherical wave [38–41]. This leads to high edge illumination of the hologram, and therefore the slots in the hologram pattern need to be narrowed towards the edges, in order to reduce the ripple caused by edge diffractions [37,50]. The narrow slots are difficult to manufacture accurately. It may happen that the narrow slots are not completely etched [68]. These narrow slots can be avoided, if the amplitude taper is already included in the field illuminating the hologram. Examples of hologram pattern slot widths of holograms designed for a corrugated feed horn and for a modified illumination are shown in Figure 3.3. A dual reflector feed system (DRFS) can be used to modify the hologram illumination to have a flat amplitude to the centre of the hologram and amplitude tapering to the edge of the hologram [25, 42]. Two DRFSs for hologram CATRs have been constructed; one at 310 GHz [12, 42] and another at 650 GHz [I–III].

Also, the quiet-zone size can be increased by using a modified illumination. As the hologram is used only for modifying the phase pattern, the width of the flat amplitude pattern in the illuminating field in principle

determines the QZ size. Traditionally the holograms have been limited to a QZ diameter less than a half of the hologram diameter, e.g. [36, 37], or up to about 65% [40]. With the modified illumination from a DRFS the QZ size is in principle proportional to the -1 dB beam-width of the illumination [25, 52].

The hologram edge illumination and the ratio of the QZ diameter to the hologram diameter are in general compromises that affect the QZ field quality, i.e. amplitude and phase ripples. The -1 dB beam-width of the illumination needs to be as wide as possible. Amplitude tapering is needed to the edge of the hologram to avoid strong diffraction from the hologram edges. The combination of a wide beam and amplitude tapering is difficult to realise with low amplitude and phase ripples and a compromise has to be made. In principle, the QZ ripples are a combination of the ripples in the illumination and the ripples caused by the hologram.

Traditionally the holograms have been limited to be used only at the linear vertical polarisation. That is because the transmission of a horizontal polarisation through the vertical slots is nearly independent of the slot width [37, 69, 70] and, therefore, edge diffraction at the horizontal polarisation is not avoided with narrowing of the slots. A hologram designed for the modified illumination from a DRFS can be used at both the vertical and horizontal polarisations [69]. However, if the hologram film is too thick, resonances inside the hologram film can prevent the use of the horizontal polarisation [III].

The hologram causes cross-polarisation due to difference in transmittance of parallel and perpendicular field components compared to the direction of the slot. With wider slots the difference of transmittance is smaller than with the narrow slots [52, 70]. With a hologram designed for horn illumination the maximum cross-polarisation level in the QZ is about -15 dB to -20 dB [12, 51]. With a hologram designed for the modified illumination from a DRFS the QZ cross-polarisation can be about $6 - 11$ dB lower [52, 70], without taking into account the cross-polarisation of the illuminating field. However, also the cross-polarisation of the illuminating field propagates to the QZ. The QZ cross-polarisation is a sum of the cross-polarisation of the illumination and cross-polarisation caused by the hologram and, therefore, the cross-polarisation level of the DRFS should be low.

3.3 Ray-tracing based synthesis method

In [I], a DRFS is designed for a 650 GHz hologram-based CATR. The DRFS is designed using a ray-tracing based numerical synthesis method [12,25,42]. This synthesis method is briefly introduced in this section and full description can be found in [12, 25, 42]. The method is similar to the method in [10], with the difference that the electromagnetic field is represented as plane waves along the rays and reflector surfaces approximated with tangential planes [12]. The synthesis starts with the chosen basic geometry and the chosen input and output fields. The second step is the definition of the input and output rays to represent the fields. Then the shapes of the reflectors are synthesised.

The geometry of a DRFS is illustrated in Figure 3.4. The geometry can be called a dual shaped hyperboloid geometry, because of the location of the focal points. The first reflector is called a subreflector and the second reflector is called the main reflector. The subreflector is directly illuminated by the feed horn and it is mainly responsible for modifying the amplitude. The main reflector is used to correct the phase. The basic geometry can be divided in three parts; the feed antenna focal point and the input field aperture plane, the system focal point F_{holo} and the output field aperture plane, and the centre ray path. The centre ray defines the distances between the feed and the reflectors and the offset angles with distances f_{sub}, r_{sub}, and r_{main} and angles α_{feed} and α_{sub}. The input and output fields are defined on the aperture planes. The angles θ_{feed} and θ_{main} affect the size of the reflectors and the edge illumination levels.

The input field is the far-field radiation pattern of the feed and the input field E_{in} on the input aperture plane is defined directly by the feed radiation pattern (2.23). Corrugated feed horns are used as feed antennas, because of the nearly rotationally symmetrical beams [12,25,42]. The input rays are launched from the feed horn phase centre point and the directions are defined by the intersection points on the input field aperture points (Figure 3.4). On the aperture plane, the rays form a ray grid of $N \times M$ rays, as illustrated in Figure 3.5. For simplicity the input field is assumed rotationally symmetric [12, 25, 42].

The output field defines the synthesis objective field E_{out}. The synthesis objective field is chosen based on the desired hologram illumination phase and amplitude distribution. Also the output field is assumed rotationally symmetric for simplicity [12, 25, 42]. The output rays are launched from

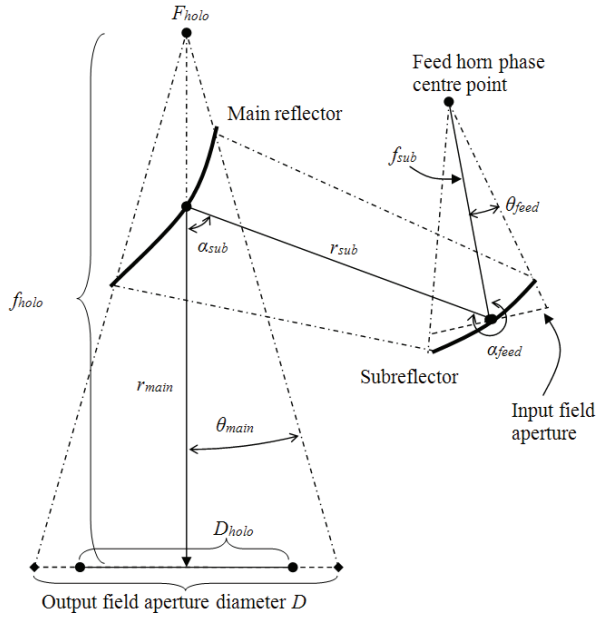

Figure 3.4. Basic geometry of a DRFS. Figure is not in scale.

the system focal point and the directions are defined by the intersection points at the output field aperture points (Figure 3.4).

The input ray points on the aperture plane are chosen. The output ray points on the aperture plane are calculated in a process called aperture mapping. The rotational symmetry simplifies the ray grid into ray rings. The ray rings are numbered from 1 to $N-1$, with n_{tube} between ray rings n and $n+1$.

The output ray coordinates are determined based on the law of power conservation inside the ray rings. Power in a ray tube n_{tube} is calculated from (2.29)–(2.30) in the input field aperture plane ray grid as

$$P_{in}(n_{tube}) \approx \frac{1}{2\eta} \frac{E_{in}^2(\rho_n) + E_{in}^2(\rho_{n+1})}{2} (\pi\rho_{n+1}^2 - \pi\rho_n^2), \tag{3.1}$$

where ρ_n and ρ_{n+1} are the input ray ring coordinates at the input aperture for ray rings n and $n+1$, respectively.

The output field is typically defined initially as a normalised amplitude function with the maximum amplitude equal to one. The output field is normalised with a scaling factor to get the total power in the input and output aperture planes equal. Next, the output ray coordinates ρ' are solved starting from the centre $\rho'_1 = 0$, by demanding that power in each ray tube is equal in the input and the output

$$P_{in}(n_{tube}) = P_{out}(n_{tube}). \tag{3.2}$$

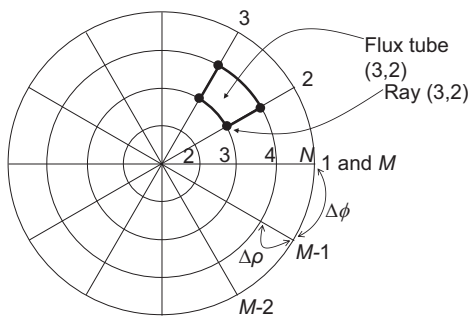

Figure 3.5. Ray grid and ray tubes.

The coordinates ρ'_{n+1} are solved from

$$P_{out}(n_{tube}) \approx \frac{1}{2\eta} \int_{\rho'_n}^{\rho'_{n+1}} E^2_{out}(\rho') 2\pi\rho' d\rho'. \tag{3.3}$$

In the numerical implementation E_{out} is initially defined in constant $\Delta\rho'$ grid (or some other user defined grid), then it is normalised with the scaling factor in order to get the total power in the input and output equal, and then (3.3) is solved for each ray tube as an integral of piece-wise continuous linear function of E^2_{out}.

When the centre ray path, input rays, and output rays are known, the reflector surfaces can be calculated. The reflector synthesis starts from the centre ray and progresses ring by ring to the aperture rim. The reflector surfaces are assumed to be locally planar given by the tangential plane calculated at the anterior point using Snell's law. For a ray (n, m) the input and output rays, the anterior points $(n-1, m)$ and the horizontal and vertical tangents at the anterior points are known. Calculation of the next point of a surface is illustrated in Figure 3.6.

The main reflector surface point is moved along the output ray to adjust the total length of the ray from the feed phase centre point to the output field aperture. The desired ray length of a ray (n, m) is

$$l(n,m) = \sqrt{\rho'^2(n,m) + f^2_{holo}} - \frac{\lambda_0}{2\pi}\Phi_{in}(n,m) - \frac{\lambda_0}{2\pi}\Phi_{out}(n,m) + C, \tag{3.4}$$

where the first term is the distance to the system focus F_{holo} (Figure 3.4), Φ_{in} is the feed antenna phase pattern, Φ_{out} is the synthesis objective phase pattern, and C is a constant that depends on the centre ray length compared to f_{holo}. After the phase correction, the ray intersection points on

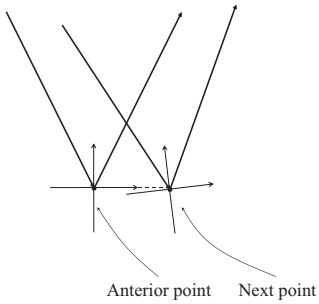

Figure 3.6. Calculation of the point on the surface using the anterior point.

both reflectors are known. Then, the tangential planes are calculated and used for the calculation of the next point.

After the synthesis, the rims of the shaped surfaces are fitted to planes with rounded sections. The rounding is needed to reduce edge diffraction. Also, the planar sections around the shaped surfaces facilitate the mechanical construction of the feed system.

Approximations in the design and error sources are [12, 25]: field polarisation is not taken into account; input (and output) fields are assumed to be rotationally symmetric causing mapping error and asymmetry to the output field; when the main reflector point is corrected to adjust the phase, also the amplitude changes and that is not taken into account in the synthesis; the synthesis does not include diffraction effects; using the anterior point tangential planes causes a cumulative error increasing towards the reflector rim; numerical accuracy depends on the number of rays; the synthesis does not take into account possible multiple reflections inside the DRFS nor does it take into account possible direct radiation from the feed to the output aperture. These approximations and limitations are taken into account and their effects minimised by the choice of the basic geometry parameters, low edge illumination of the reflectors, and by using the synthesis method together with simulations that take into account, e.g., non-symmetry of the feed radiation pattern and cross-polarisation.

As part of the design procedure, used in designing both the 310 GHz DRFS [12] and the 650 GHz DRFS [I], the optimisation of the DRFS is based on iterative process including reflector synthesis and simulations using physical optics (PO) to verify the operation of the synthesised DRFS. These two successfully designed DRFSs show that the synthesis method can be used to design shaped reflector antennas.

3.4 Design of a 650 GHz dual reflector feed system

In [I], a dual reflector feed system is designed for a 650 GHz hologram-based compact antenna test range. The reflector synthesis method based on ray-tracing, introduced in Section 3.3, is used together with iterative optimisation with a commercial reflector antenna simulation software GRASP8W [71] using physical optics (PO) and physical theory of diffraction (PTD).

The design objective is a hologram illumination at linear vertical polarisation for a hologram with $f_{holo}/D_{holo} = 4$, a -1 dB beam-width corresponding to an (at least) 2-m-diameter QZ with the 3-m-diameter hologram, and a -10 dB amplitude tapering to the hologram edge.

The input field in the synthesis is the simulated radiation pattern of the corrugated feed horn with a Gaussian beam with -30 dB half-beam width is about 30°. The output field amplitude is defined as a Butterworth-type function

$$E(\rho') = \frac{1}{\sqrt{1 + (\rho'/\rho'_c)^{2N}}}, \tag{3.5}$$

where ρ' is the output field aperture coordinate, ρ'_c is the half power (-3 dB) point, and N is the degree of the Butterworth function. The output field aperture is larger than the hologram (Figure 3.4). The edge illumination levels at the subreflector (about -27.5 dB) and main reflector (about -35 dB) edges and also the output field pattern outside the hologram are found to be important in reducing diffraction ripples in the hologram illumination.

The -1 dB beam-width should be as large as possible because it effectively determines the QZ diameter. The difference between the synthesis objective and the PO simulated beam is increasing as a function of the attempted beam-width of the synthesis objective field. It was found that by optimising the phase pattern of the output field synthesis objective the realisable beam-width can be increased.

A 3-D model of the designed 650 GHz DRFS structure is illustrated in Figure 3.7. The simulation results are presented in [I, II]. The simulated DRFS beam corresponds well to the desired hologram illumination. The simulated amplitude ripple is 0.45 dB peak-to-peak, phase deviation from spherical wave is 5° peak-to-peak, the hologram edge illumination is under -10 dB, and the cross-polarisation level is -21 dB at maximum.

The designed 650 GHz DRFS has a wider beam and better beam quality than the 310 GHz DRFS [12] despite the higher frequency. The most

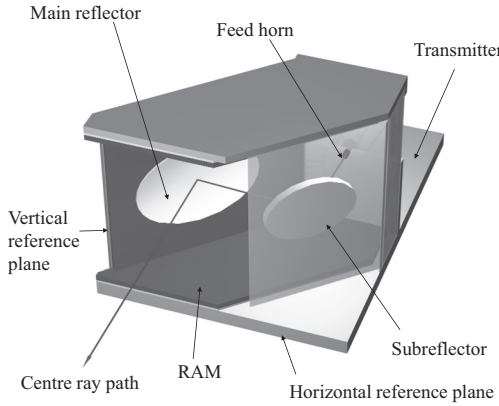

Figure 3.7. A 3-D model of the 650 GHz DRFS structure. [25]

important reasons for this are the optimisation of the synthesis objective phase pattern and the lower reflector edge illumination levels. Edge illuminations were chosen to be -27.5 dB and -35 dB, for the subreflector and main reflector, respectively, instead of the -15 dB for both reflectors in the 310 GHz DRFS design [12]. In the 310 GHz DRFS design the parameters of the Butterworth function (3.5) were $N = 5$ and $\rho_c = 70\%$ of the hologram radius [12] and with the 650 GHz DRFS the same parameters are $N = 10.7$ and $\rho_c \approx 85\%$ of the hologram radius. The wider beam would not have been possible without optimisation of the synthesis objective phase pattern.

3.5 Testing of a 650 GHz dual reflector feed system

The 650 GHz DRFS is measured by near-field scanning with a planar scanner in [II]. The measurement is done to ensure that the DRFS is designed and manufactured successfully.

The most significant phase measurement error source in a submillimetre wave planar near-field measurement is the scanner planarity [72]. Using the usual phase measurement error correction techniques results in a phase pattern result that depends on which area of the scanning plane is used. Measured phase deviation results in Figure 3.8, after drift correction with tie-scans and planarity error correction based on measured planarity data, show that the phase measurement accuracy is not good enough with the standard techniques. In [II], a planarity error correction technique, in which a corrected scanner planarity data are calculated

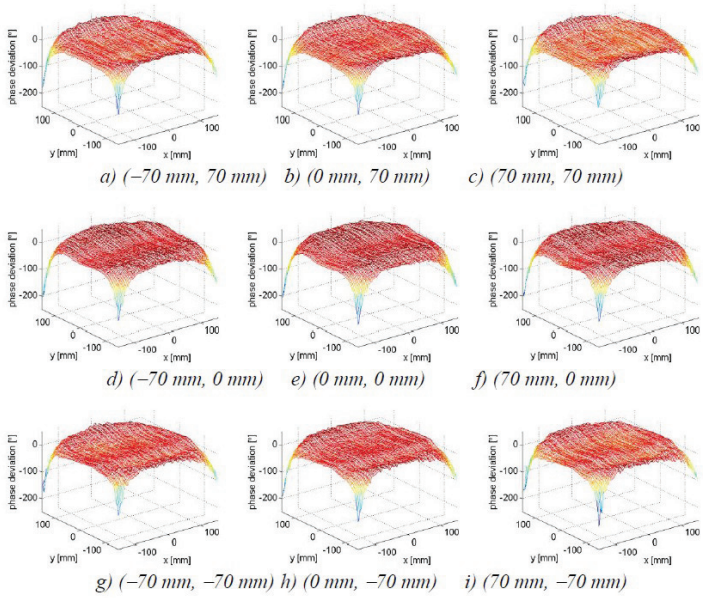

Figure 3.8. Measured 650 GHz phase deviation from a spherical wave front with planarity correction based on the laser tracker using different areas of the scanning plane; a) – i) offsets (x, y) of the measurement areas. Location of the focal point is calculated separately for each of these measurements. [25]

from measured phase patterns with partially overlapping scanning areas, is used. The main disadvantage of this method is that it requires several measurements, but it enables meaningful comparison to the simulated pattern.

The measured -1 dB beam-width and hologram edge illumination level corresponds well to the simulated one. The measured cross-polarisation level is about -14 dB. The measured ripples in the central region of the beam are about ± 0.8 dB peak-to-peak and about $\pm 15^\circ$ peak-to-peak in amplitude and phase deviation, respectively. Although these measured ripples are larger than the simulated, the field quality is considered good enough.

3.6 Antenna tests at 650 GHz

A 650 GHz hologram-based CATR is designed, constructed, and used to test a 1.5-m diameter antenna in [III]. The DRFS designed in [I] and tested in [II] is used to provide the desired modified illumination for the hologram. Before the antenna tests the QZ was measured and optimised.

The antenna under test is a single parabolic offset reflector ADMIRALS RTO [41, 45, 65, 73].

The location and orientation of the DRFS is optimised based on QZ measurements for the best possible QZ quality. The QZ field is probed by placing the receiver on a plane polar scanner positioned on top of the antenna positioner prior to the antenna tests. The planarity of the scanner is measured with a tracking laser interferometer. The QZ size corresponds well to the designed value. In the region of the AUT, the measured field deviations are 3 dB and 270° peak-to-peak in amplitude and phase, respectively. The main reason for the large scale phase deviations is considered to be uneven stretching of the hologram. Due to insufficient QZ scanner planarity and repeatability, accurate analysis of the QZ field quality is not possible and effects on the antenna measurement results cannot be estimated reliably.

The RTO is measured traditionally by rotating the AUT in the QZ and also by range feed scanning. With the feed scanning technique the main beam region is measured by moving the DRFS, i.e. by tilting the QZ phase. The measured patterns are similar with both methods. Large field cuts are measured by rotating the AUT. Spurious side lobes are identified and corrected using feed scanning antenna pattern comparison technique (APC). Also, the cross-polarisation pattern is measured. The measured cross-polarisation maximum of -24 dB, clearly higher than the simulated -35 dB, is most likely caused by the relatively high QZ cross-polarisation level of about -25 dB.

The measured pattern is compared to a simulated pattern. The RTO is simulated with PO and PTD using physically measured reflector surface data. The measured and the simulated radiation patterns agree reasonably well to each other. Comparison of measured and simulated E-plane cuts are presented in Figure 3.9. The differences between the measured and simulated patterns are caused by the non-ideal QZ field and the inaccuracies of the simulation model (probably more due to the non-ideal QZ phase because of the higher peak-to-peak deviations in the QZ compared to the estimated aperture phase pattern uncertainty in the RTO simulation [III]). These antenna tests show the potential usability of hologram-based CATR for antenna tests at submillimetre wavelengths.

The RTO was tested previously at 322 GHz in a hologram-based CATR [40, 41]. In comparison, in the 650 GHz tests the main differences were the higher frequency and QZ phase measurement accuracy. Due to the

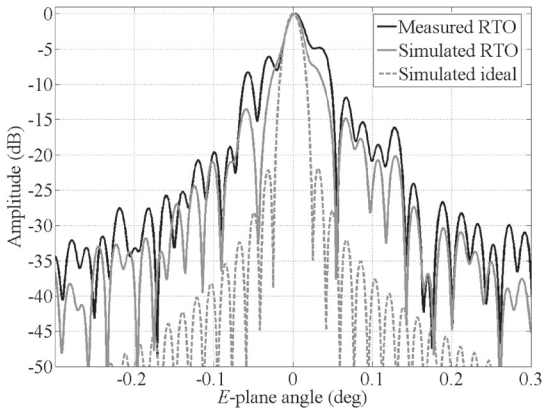

Figure 3.9. Measured E-plane cut (black), the simulated E-plane cut of the RTO (gray), and the simulated E-plane cut of an ideal paraboloid of same size (gray dash). [III]

higher frequency the mechanical accuracies of the QZ scanner and the hologram are more critical as the scanner planarity, scanner planarity measurement, hologram pattern, antenna surface shape, etc. have accuracy requirement directly relative to the wavelength. In the tests at 322 GHz [41], the QZ scanner planarity, repeatability, and the planarity measurement accuracy compared to the wavelength were sufficient to enable good estimation of the effects of the non-ideal QZ field on the measured pattern.

3.7 Discussion and future work

The design and test results of the 650 GHz DRFS show that the synthesis method is well suited for designing a feed system for a CATR. One possible improvement in future would be to include accurately measured radiation pattern of the feed horn in the DRFS design.

The antenna tests at 650 GHz showed that the hologram-based CATR has good potential for antenna tests at submillimetre wavelengths. The main problems in the conducted measurement campaign can be identified as insufficient scanner planarity in the QZ measurement, hologram stretching affecting the QZ phase, and the relatively high cross-polarisation level in the QZ. The QZ scanner repeatability problem could be solved by conducting the planarity scanning and QZ measurements simultaneously. Improvement of the QZ cross-polarisation level could be achieved

by designing the feed system and the hologram together. It might be possible to design a compensated range similarly as what is common with reflector-based CATRs.

4. Beam-steering integrated lens antennas (ILAs)

In an integrated lens antenna (ILA), a feed antenna is integrated into direct contact with a rotationally symmetric dielectric lens [28, 29, 74, 75]. Another name for ILA is a substrate lens [74,75]. As the feed is integrated into direct contact with the lens, it offers mechanical rigidity, thermal stability, elimination of substrate modes, and good coupling to the lens. The lens has an elliptical, e.g. [30,33,76–80], [VI,VII,X,XI], or a hemispherical, e.g. [7, 26, 28, 29, 76, 81–83], [IV–IX], surface that collimates the radiation from the feed. Electrical beam steering is possible with a feed array and a switching network [82, 83], [V,VII]. ILA and the beam-steering principle are illustrated in Figure 4.1. Only one of the feed elements is used at the time and the direction of the main beam depends on the location of the active feed element.

Beam-steering ILAs are studied and developed in this thesis [IV–XI]. The work is focused on demonstrating electrical beam-steering [V,VII], improvement of beam properties with large beam-steering angles [VI,VII, IX], comparison of different lens permittivities with different feed ele-

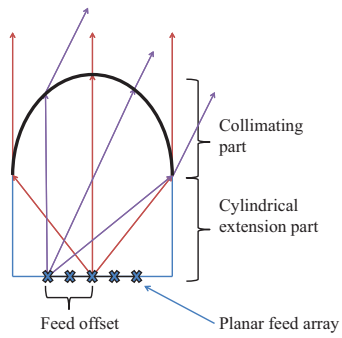

Figure 4.1. Typical ILA geometry and an illustration of the beam-steering principle. Feed offset is defined as the feed element distance from the rotational symmetry axis of the lens. [XI]

ment directivities [IV,VI,VIII, IX,XI], and reduction of internal reflections [VIII–XI]. Several prototypes are manufactured and tested with antenna measurements at 77 GHz [V,VII–X].

Possible applications that are considered for the developed ILAs are either a beam-steering link antenna for E-band (71 GHz – 86 GHz) telecommunication applications or perhaps an automotive radar antenna (77 GHz – 81 GHz). In principle, a beam-steering ILA can be used to provide the desired electrical beam steering with a narrow diffraction limited beam.

The ILAs are designed and analysed with ray-tracing simulations. The ray-tracing lens simulations are introduced in Section 4.1. Conventional ILAs and electrical beam-steering demonstration with an extended hemispherical Teflon lens are presented in Section 4.2. Methods aiming at improving the beam-steering properties with large offsets are discussed in Section 4.3. Lens shaping methods are developed for reducing harmful internal reflections in Section 4.4.

4.1 ILA simulation with ray-tracing

Electrically large ILAs are commonly simulated using ray tracing, e.g. [7, 26, 28–30, 33], [IV–XI]. The fields outside the lens are calculated using ray tracing from the feed. The far-field is solved from the near-field of the lens using Huygens' method, i.e., aperture integration of equivalent surface currents. Ray-tracing uses Snell's law on the lens surface and the power conservation law inside elementary ray tubes. Sometimes this method is called geometrical optics (GO) and physical optics (PO), or GO/PO-method, e.g., in [7].

The feed is modelled as a point source located at the phase centre. The feed antenna far-field radiation pattern is used to determine the initial values for the fields along the rays. The feed radiation pattern is typically a simulated far-field pattern into a half-space filled with the lens material, e.g., in [7, 26, 26, 28, 29], [V,VII,VIII,X,XI]. It is also possible to define the feed radiation pattern with some simple equation [30], [IV,VI–IX,XI].

The total power in different field components are calculated as the sum of the powers in all of the ray tubes. The total power radiated from the feed into the lens P_{tot}, reflected P_{refl}, spillover P_{spill}, and dielectric loss P_{diel} are compared to calculate different loss factors. The reflection loss is defined as

$$L_{refl} = 10 \cdot \log_{10}(P_{tot}/(P_{tot} - P_{refl})). \tag{4.1}$$

P_{spill} is the total power leaking out from the extension part of the lens. Spillover loss is defined as

$$L_{spill} = 10 \cdot \log_{10}(P_{tot}/(P_{tot} - P_{spill})). \tag{4.2}$$

The dielectric loss P_{diel} is the power loss due to dielectric loss between the feed and the lens surface. Dielectric loss is defined as

$$L_{diel} = 10 \cdot \log_{10}(P_{tot}/(P_{tot} - P_{diel})). \tag{4.3}$$

The reflected rays can be traced and the effects of the reflections to the far-field can be calculated as, e.g., in [26, 30],[V]. Ray tracing does not accurately reproduce specific side-lobes but can be used to predict the general side-lobe level increase due to the reflections [26]. In this thesis, the reflections are analysed only by considering the reflection loss (except in [V]) for two reasons. Simulating the effects of the internal reflection does not reduce those effects. It is considered more important to reduce L_{refl}. The second reason is that in simulation the reflections take a lot of computing time and, therefore, the main advantage of simple and fast ray-tracing simulation is at least partly lost.

Once the rays and fields have been calculated outside the lens, the far-field is solved with Huygens' method, i.e., aperture integration of equivalent surface currents. The equivalent electric J_s and magnetic M_s surface currents are

$$\overline{J}_s = \overline{n} \times \overline{H} \tag{4.4}$$

$$\overline{M}_s = -\overline{n} \times \overline{E}, \tag{4.5}$$

where $\overline{n}$ is the integration surface normal vector. Effectively, only the tangential components of the electric $\overline{E}$ and magnetic $\overline{H}$ fields are used. The equivalent surface currents replace the original antenna problem and the field outside the lens is integrated from the currents. Typically, the far-field is calculated from equivalent surface currents on the lens surface, e.g. [26, 28–30] , [IX,XI]. In [IV–VIII,X], the equivalent currents are calculated on a surface that is perpendicular to the rays (Figure 4.2) and the fields are tangential to the aperture surface. Therefore, it is not necessary to calculate the projection to the surface. Using the different integration surfaces result in slightly different radiation patterns. In principle, the integration surface can be chosen to be any surface, on which it is convenient to make assumptions regarding the field values [35].

Ray illustration of Teflon ($\varepsilon_r = 2.1$) and silicon ($\varepsilon_r = 11.7$) lenses are presented in Figure 4.2. Similar ray illustrations are used in [IV–XI].

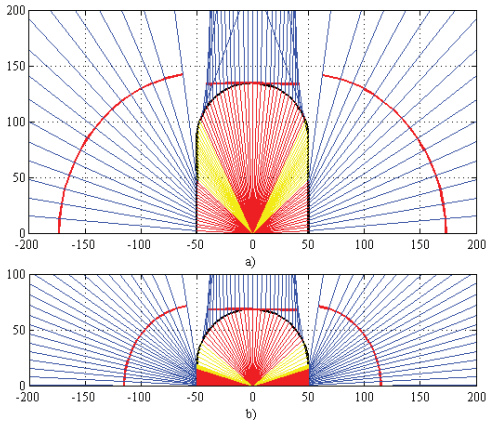

Figure 4.2. Rays in a) Teflon ($\varepsilon_r = 2.1$) and b) silicon ($\varepsilon_r = 11.7$) lenses with the optimised extension lengths. Yellow rays are totally reflected. The red line outside the lens is the optional integration surface that is perpendicular to the rays. [IV]

The internal reflections are known to cause high side-lobes, increased cross-polarisation level, effects on input impedance of the feed, and mutual coupling [26, 30, 77–79], [V,VII–XI]. With offset feeds the reflection loss can be close to 50% or even more and it is mostly due to total reflections. Methods for reducing the reflections by lens shaping developed in this thesis are discussed in Section 4.4. The reduction of internal reflections is mainly based on reduction of total reflections at the lens extension [VII,XI]. Therefore these fields get out from the lens and become part of spillover loss. Total loss does not change and, therefore, the antenna gain is not improved.

The directivity and total losses, i.e., gain, depends mostly on the lens shape, feed element directivity, and feed offset. Properties of ILAs with a wide range of different lens permittivities and feed element directivities are studied with the conventional and with the proposed lens designs [IV–XI].

4.2 Conventional ILAs

In [IV], large extended hemispherical ILAs are compared with ray-tracing simulations. Different lens permittivities ($\varepsilon_r = 2.1$, 3.8, and 11.7) are compared. The simulations are done for a 100 mm diameter antennas at 77 GHz. A simplified feed radiation pattern is used that enables a simple control of the feed element directivity. The feed radiation pattern is con-

sidered to be a point source with an amplitude pattern of

$$|\overline{E}(\phi,\theta)| = cos^N(\theta), \quad 0 \leq \theta \leq 90^\circ, \quad 0 \leq \phi \leq 360^\circ, \tag{4.6}$$

at the main polarisation of Ludwig's second definition of polarisation [84]. The directivity of the feed element is varied with the parameter N. The same simplified feed radiation pattern is used in [IV,VI–IX,XI].

The cylindrical part of the lens is called an extension (Figure 4.1). The extension length for different lens materials is optimised for maximum directivity. The extension length that gives the maximum directivity does not depend on the feed directivity. The field leaking out from the extension increase the side-lobe level and decrease the directivity.

It is found that the reflection loss is high with medium feed directivities with any extended hemispherical lens with any lens material. Lower reflection losses are possible with 1) low permittivity lens with low directivity feed, 2) medium or 3) high permittivity lens and high feed directivity. Beam-steering properties are studied with the optimum extension lengths and selected feed directivities as a function of the feed offset. The half-power beam-width, reflection loss, and maximum beam-steering angle (limited by reflection loss) are nearly identical for all three options. With low permittivity lens the required feed element spacing is the largest, thus the mutual coupling between the feed elements is expected to be the lowest.

4.2.1 Electrical beam-steering demonstration

In [V], a 100-mm diameter extended hemispherical Teflon ($\varepsilon_r = 2.1$) lens and an 8-element patch antenna array on low temperature co-fired ceramic (LTCC) is fabricated and tested at 77 GHz. Switching array with one SPDT-type switch and two SP4T-type switches are used to select the active feed element. The lens dimensions are chosen based on [IV]. Radiation patterns are measured with planar near field measurements.

The feed antennas are in a linear configuration in the H-plane direction with a pitch of 3 mm. The beam-width is about 2° for the on-axis feed and about 2.5° for the 21 mm off-axis position. The measured radiation patterns clearly demonstrate the beam steering. Measured and simulated radiation patterns are compared with feed element offsets of 0 mm and 21 mm in Figure 4.3.

4.3 Performance improvement for large beam-steering angles

With large feed offsets from the optical focus of the lens, i.e., large beam-steering angles, the focusing properties deteriorate and losses increase. Methods aiming at improving the beam-steering properties with large offsets are discussed in this section. Two different approaches for improving the performance with large beam-steering angles are presented in [VI, VII] and [IX].

4.3.1 Optimised eccentricity lens

With low permittivity lens materials, conventional integrated lens types, i.e. extended hemispherical and the elliptical lenses, have different beam-steering characteristics. In [VI], the role of the lens eccentricity is studied with ray-tracing simulations. The eccentricity of the collimating part of an elliptical (or an extended hemispherical) ILA is defined as

$$e = \sqrt{1 - (b/a)^2}, \tag{4.7}$$

where a is the semimajor axis of the ellipse and b is the semiminor axis of the ellipse, i.e., the radius of the lens. The conventional elliptical ILA has $e = (\varepsilon_r)^{-1/2}$, and its extension length L equals $e \cdot a$. The extended hemispherical lens has eccentricity of 0.

Lenses with different eccentricities are simulated and compared. The extension length is optimised for each eccentricity. It is found that the optimal eccentricity for a Rexolite ILA ($\varepsilon_r = 2.53$) is an intermediate value of about 0.78 times the eccentricity of a conventional elliptical lens. With the intermediate eccentricity, directivity is nearly constant up to large beam-steering angles ($> 20°$).

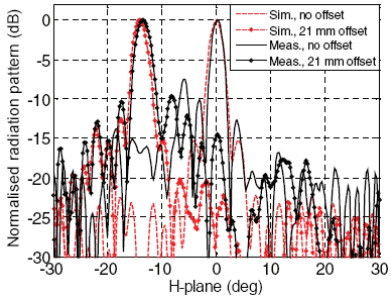

Figure 4.3. Normalised measured and simulated radiation patterns. The feed element offsets are 0 mm and 21 mm. [V]

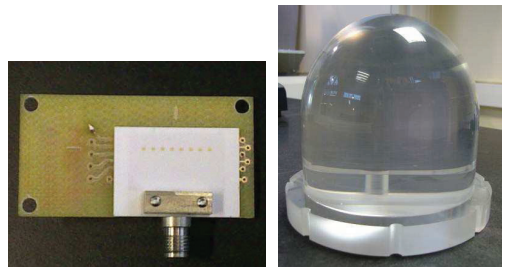

Figure 4.4. Photographs of the LTCC feed array attached to a circuit-board and the designed 100-mm diameter Rexolite lens. [VII]

In [VII], an optimised eccentricity Rexolite (ϵ_r = 2.53, tan δ = 0.0013 in W-band [85]) lens and an 8-element feed array on LTCC is made and tested at 77 GHz. Photograph of the lens and the feed array is presented in Figure 4.4. Scan loss, main-beam width and direction, side-lobe levels, directivity, and cross-polarisation are analysed in detail with both simulations and radiation pattern measurements.

The measured half-power beam-width at 77 GHz is $2.5° \pm 0.2°$ up to the largest tested beam-steering angle of $30°$. The low permittivity lens with the optimised eccentricity results in a smaller scan loss than the conventional lenses.

Because of the internal reflections, the side-lobes and cross-polarisation level outside the main-beam region increase compared to those simulated without the reflected fields. However, these results show that the lens shape can be optimised with ray-tracing simulations provided that the reflection losses are also taken into account in the comparison of different lens shapes.

4.3.2 Lens with feeds on a spherical surface

In [IX], an extended hemispherical ILA is presented with the feed antennas placed on a spherical surface instead of the conventional planar one. As the feeds are on the spherical surface, with the radius equal to the extension length, the lens geometry becomes symmetrical and results in a very low scan loss. A prototype is tested at 77 GHz. The designed lens prototype is based on the 100-mm diameter extended hemispherical Teflon lens [V]. Later, the internal reflections were reduced by shaping the extension [VIII] (Section 4.4.1), and an absorber was placed around the shaped extension to capture the spillover fields [X]. The lens is illustrated in Figure 4.5.

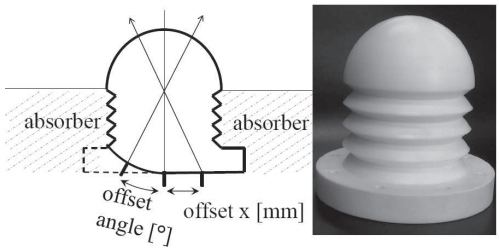

Figure 4.5. An illustration of the beam-steering principle with an integrated lens antenna with feeds on spherical or planar surface (lhs.). Photograph of the Teflon lens used in the measurements (rhs.). One side of the bottom of the lens was modified to enable measurement of feed positions on a spherical surface. [IX]

The measurement results in [IX] show that the gain is within 1 dB up to about $25°$. Also, the beam shape is nearly equal and side-lobe levels are low.

Lenses with relative permittivities from 2 to 12 are compared with ray-tracing simulations. Small scan loss is possible with any permittivity and any feed directivity up to about $25°$. The main differences are found to be lower gain with low-permittivity lenses, shorter distance between the feed elements with the high-permittivity lenses, and greater degree of freedom to design the shape of the extension for minimised reflections with low permittivity lens.

4.4 Reduction of internal reflections

Methods for reducing the reflections by lens shaping developed in this thesis are discussed in this section. Reflections can also be reduced by covering the lens with a matching layer (not effective against total reflections as the critical angle for total reflections remains the same), by using very high directivity feed elements (lower efficiency due to only a small part of the aperture is illuminated and not practical for feed arrays where the feed elements are close to each other), lens material with high dielectric losses (increasing losses), or by using lower extension length (does not produce diffraction limited beams).

4.4.1 Extension shaping of low permittivity ILA

With low permittivity extended hemispherical ILA most of the reflection loss comes from total reflections at the extension. In [VIII] it is proposed

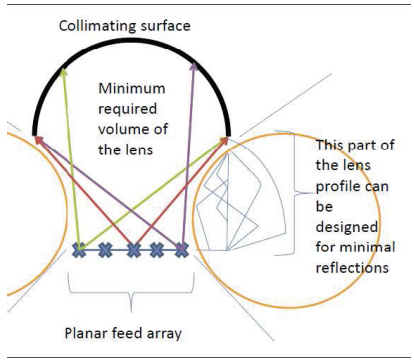

Figure 4.6. The design principle of the proposed method for reduction of internal reflections. The lens shape between the feed array and the collimating surface is designed for minimal total reflections. [VIII]

that the shape of the extension can be designed for minimising total reflections. The design principle is illustrated in Figure 4.6.

The Teflon lens from [V] is used to demonstrate the reduction of internal reflections. New extension shape is designed (Figure 4.5). It is shown with ray-tracing simulations that the reflection loss is low with the shaped extension. It is shown with measurements that the reflected power coming back to the bottom of the lens is decreased and with large feed offsets the side lobes are lower. The side-lobe levels in general remain the same.

In [IX,X], absorber is placed around the shaped extension of the Teflon lens designed in [VIII]. Because of the shaped extension, the fields that go to the extension are directed out from the extension in a controlled manner, instead of a strong total reflection that produces the high side lobes. As the spillover field goes to the absorber, it is possible to have low side-lobe levels even with feed offsets.

4.4.2 Lens shaping of elliptical ILA

In [XI], a lens shaping principle is presented that can be used to design an elliptical ILA with low reflection loss, with moderate beam-steering angles, using any relative permittivity of the lens and any feed element directivity. The design principle is illustrated in Figure 4.7. Only a radius of $R \leq b$ of the ellipse is used and the rest of the lens is shaped in order to avoid total reflections and absorber is placed around the extension to capture the spillover field.

An elliptical Rexolite ILA, designed based on principles presented in [XI], is tested with antenna measurements at 77 GHz in [X] and compared

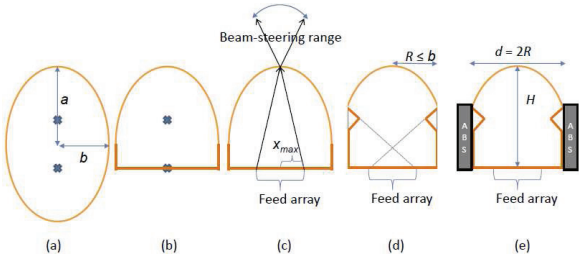

Figure 4.7. Illustration of conventional lens (a)-(c) and proposed method for reduction of internal reflections (d)-(e). [IX]

to ray-tracing and FDTD simulations [X,XI]. The designed lens has low reflection loss and low side-lobe levels. It is shown that with a good lens, i.e. when reflections are minimised, the accuracy of ray-tracing simulation is also good. In addition, ILA for two-dimensional beam-steering with a non-symmetrical beam is studied and compared to the rotationally symmetric lens [X].

In [XI], the shaped elliptical ILAs with different lens permittivities and feed element directivities are compared with ray-tracing simulations based on reflection loss, lens shape, gain, directivity, beam-width, and the resulting distance between the feed elements. Simulation results are given for $20 \times \lambda_0$-diameter ILAs designed for a beam-steering range of approximately $\pm 15^\circ$. Low reflection loss ($L_{refl} < 1$ dB) is easily achieved with low and medium lens permittivities without any matching layer. A high-permittivity lens requires larger b/R and a matching layer to the extension. Higher gain is achieved with higher feed directivities and higher lens permittivities, mostly due to differences in spillover losses. On the other hand, the distance between the feed elements is smaller with higher lens permittivities. Especially with high directivity feeds, the distance between the feed elements is very small compared to the diameter of the feed element effective area.

4.5 Discussion and future work

The next step is to design and test an ILA with two-dimensional beam-steering. Plans have been done for a 64-beam electrical beam-steering antenna system. The idea of placing the feed elements on a spherical surface of a extended hemispherical lens will be further studied and feed arrays will be studied.

The advantages and disadvantages of low and high permittivity lenses are studied in this thesis. The most important open question is how the effects of mutual coupling between the closely spaced feed elements depend on the feed element directivity and resulting spillover losses.

5. Summary of articles

Publication I: "Design of a 650 GHz dual reflector feed system for a hologram-based CATR"

The 650 GHz dual reflector feed system (DRFS) is designed. The antenna parameters are optimised with ray-tracing synthesis method and simulations with physical optics. Low levels of simulated amplitude and phase ripples are achieved for the hologram illumination field. The key factors are found to be minimised edge illumination, proper selection of the desired output field amplitude, and optimisation of the output field phase pattern in the synthesis.

Publication II: "Antenna measurement at 650 GHz with a planar near-field scanner"

In this publication the 650 GHz DRFS is tested with near-field antenna measurements. Planarity error compensation technique is used enabling correction to the measured phase without accurate pre-existing information of the planarity error of the planar near-field scanner. It is concluded that the 650 GHz DRFS has been successfully designed and manufactured.

Publication III: "Antenna tests with a hologram-based CATR at 650 GHz"

A hologram-based compact antenna test range (CATR) is designed, constructed, and used to test a 1.5-m antenna at 650 GHz. A 3.16-m diameter hologram and a dual reflector feed system (DRFS) are designed and constructed for these measurements. The DRFS, designed in [I] and tested in [II], is used successfully in a full scale compact range to provide a modified illumination for the hologram. The measured radiation patterns of

the antenna under test agree reasonably well with the simulated ones. The hologram-based CATR and the results of the antenna tests at 650 GHz presented in this paper show that a hologram-based CATR can be used for testing large antennas at submillimetre wavelengths.

Publication IV: "A study of extended hemispherical lenses for a high-gain beam-steering antenna"

Large extended hemispherical integrated lens antennas (ILAs) with different permittivities are compared with ray-tracing simulations. It is shown how the directivity and the power coupling to internal reflections, i.e., the reflection loss, depend on the lens permittivity, the feed element directivity, and the beam-steering angle. The most promising combinations of lens permittivity and feed directivity are reported.

Publication V: "Mm-wave lens antenna with an integrated LTCC feed array for beam steering"

Electrical beam steering is demonstrated using a large Teflon extended hemispherical ILA. An 8-element patch feed antenna array with a switching network is designed and manufactured with low temperature co-fired ceramic (LTCC) technology. Beam steering is tested with radiation pattern measurements at 77 GHz.

Publication VI: "Optimal eccentricity of a low permittivity integrated lens for a high-gain beam-steering antenna"

The role of eccentricity of the collimating part of a low-permittivity ILA for beam-steering is studied with ray-tracing simulations. Considering the resulting compromise between reflection loss, directivity, and beamwidth, the optimal eccentricity is concluded to be an intermediate value between those of the conventional extended hemispherical and the elliptical lenses.

Publication VII: "Using optimized eccentricity Rexolite lens for electrical beam steering with integrated aperture coupled patch array"

An optimised eccentricity Rexolite ILA is made and tested. An 8-element aperture coupled patch antenna feed array with a switching network is integrated in LTCC. The lens shape is optimised in [VI] for improved

beam-steering properties for a large angular range. The designed optimised eccentricity lens is compared with simulations to the conventional extended hemispherical and elliptical lenses. It is shown that the optimised eccentricity lens results in smaller scan loss than the conventional low permittivity lenses. The lens is tested with the LTCC feed array at 77 GHz. The beam-steering properties, including scan loss, main-beam width and direction, side-lobe levels, directivity, and cross-polarisation are analysed in detail.

Publication VIII: "Reduction of internal reflections in low permittivity integrated lens antennas"

In this paper, a new and simple method, which significantly reduces the internal reflections in a low permittivity ILA for beam-steering is proposed. The method is based on designing the lens extension for minimal reflections instead of using the conventional cylindrical extension. A shaped extension is designed for the extended hemispherical Teflon lens presented in [V] and analysed with ray-tracing simulations and antenna measurements. Simulations and measurements show that the internal reflections are significantly reduced with the designed shaped extension compared to the original conventional cylindrical extension.

Publication IX: "Extended hemispherical integrated lens antenna with feeds on a spherical surface"

A prototype ILA is presented and demonstrated to exhibit low scan loss and low side-lobe levels with larger beam-steering angles than in case of a conventional lens design. The lens is based on the extended hemispherical Teflon lens presented in [VIII], with the difference that the feed elements are placed on a spherical surface, instead of a conventional planar one. This results in a symmetric design and nearly identical beams up to about $20^\circ - 25^\circ$ beam steering angles. The proposed lens design is also studied with ray-tracing simulations for different lens permittivities.

Publication X: "2D beam-steering with non-symmetrical beam using non-symmetrical integrated lens antenna"

An integrated lens antenna design allowing two-dimensional beam-steering with a non-symmetrical beam with low reflection losses and low side-lobe levels is proposed. Prototypes are designed and tested with antenna

measurements.

Publication XI: "Reduction of internal reflections in integrated lens antennas for beam-steering"

The method for reducing the internal reflections in ILAs introduced in [VIII] is generalised for any lens permittivity. ILAs with wide ranges of realistic relative permittivity of the lens and of the feed element directivity are designed with ray-tracing simulations. It is shown that with any permittivity and with any feed directivity it is possible to design the lens shape in such a way that, for moderate beam-steering angles, the reflection loss is low without resorting to a complicated matching layer. The effects of the antenna parameters on the reflection loss, gain, and on the distance between the feed elements are presented and analysed in detail.

6. Conclusions

In this thesis, ray tracing is used in designing millimetre and submillimetre wave antennas. Ray tracing is used both in antenna synthesis as well as in antenna simulations. Several antennas are designed and tested with antenna measurements. This thesis consists of two parts. In the first part, a 650 GHz dual reflector feed system (DRFS) is designed, tested, and used in a hologram-based compact antenna test range (CATR). The second part focuses on the design of electrically beam-steerable millimetre wave integrated lens antennas (ILAs).

The 650 GHz DRFS is designed using ray-tracing based synthesis method. The DRFS is used in a hologram-based CATR to provide the desired modified illumination. The feed system is tested with planar near-field measurements. The 650 GHz hologram-based CATR is designed, constructed, and used to test a 1.5-m diameter antenna.

In the second part of this thesis, several beam-steering ILAs are designed. Two ILAs with integrated feed arrays and switching networks are used to demonstrate electrical beam steering at 77 GHz. The work focuses on improving the beam-steering properties of the ILAs and on the reduction of the unwanted high side-lobes caused by internal reflections. Several low permittivity ILAs are designed and tested with antenna measurements. Furthermore, different lens permittivities and feed element directivities are studied and compared using ray-tracing simulations.

Typically, at large beam-steering angles the gain of an ILA decreases. In this thesis, the eccentricity of a low-permittivity ILA is optimised aiming for improvement of the beam properties for large beam-steering angles. It is shown that by placing the feeds of an extended hemispherical lens on a spherical surface it is possible to have very low scan loss up to large beam-steering angles.

Simple and effective lens shaping method is developed. The method can

be used to design ILA with small reflection loss. Furthermore, it is shown with ray-tracing simulations that it is possible to design an ILA with low reflection loss using any lens permittivity and any feed element directivity. Low permittivity extended hemispherical and elliptical ILAs are designed, fabricated, and used to demonstrate good beam-steering properties with low side-lobes.

Bibliography

[1] http://www.rssd.esa.int/index.php?project=PLANCK

[2] *ETSI TS 102 524, Fixed Radio Systems; Point-to-Point equipment; Radio equipment and antennas for use in Point-to-Point Millimetre Wave applications in the Fixed Services (mmwFS) frequency bands 71 GHz to 76 GHz and 81 GHz to 86 GHz*, July 2006, 19 p.

[3] R. R. Rasshofer and K. Naab, "77 GHz long range radar systems status, ongoing developments and future challenges," *Proceedings of the 2nd European Radar Conference*, Paris, France, Oct. 6–7, 2005, pp. 161–164.

[4] R. E. Collin and F. J. Zucker, *Antenna Theory, part 2*, Inter-University Electronic Series, vol. 7, McGraw-Hill Book Company, New York, United States of America, 1969, 683 p.

[5] I. Lindell and K. Nikoskinen, *Antenniteoria* (in Finnish), Otatieto, no. 848, Helsinki 1997, 347 p.

[6] G. A. Deschamps, "Ray tracing in electromagnetics," *Proceedings of the IEEE*, vol. 60, no. 9, pp. 1022–1035, Sept. 1972.

[7] N. T. Nguyen and R. Sauleau, "Improvement of the GO/PO method for the study of focal array fed lens antennas," *Proceedings of the European Conference on Antennas and Propagation (EuCAP 2009)*, Berlin, Germany, March 23–27, 2009, pp. 3003–3006.

[8] C.-F. Yang, B.-C. Wu, and C.-J. Ko, "A ray-tracing method for modeling indoor wave propagation and penetration," *IEEE Transactions on Antennas and Propagation*, vol. 46, no. 6, pp. 907–919, June 1998.

[9] T.-S. Wang and C.-F. Yang, "Simulations and measurements of wave propagations in curved road tunnels for signals from GSM base stations," *IEEE Transactions on Antennas and Propagation*, vol. 54, no. 9, pp. 2577–2584, Sept. 2006.

[10] P.-S. Kildal, "Synthesis of multireflector antennas by kinematic and dynamic ray tracing," *IEEE Transactions on Antennas and Propagation*, vol. 38, no. 10, pp. 1587–1599, Oct. 1990.

[11] P.-S. Kildal, "Analysis of numerically specified multireflector antennas by kinematic and dynamic ray tracing," *IEEE Transactions on Antennas and Propagation*, vol. 38, no. 10, pp. 1600–1606, 1990.

[12] J. Häkli, *Shaped Reflector Antenna Design and Antenna Measurements at sub-mm Wavelengths*, Doctoral Thesis, Helsinki University of Technology, Espoo, Finland, 2006, 217 p.

[13] I. Lindell, *Radioaaltojen eteneminen* (in Finnish), Otatieto, no. 841, Helsinki 2000, 261 p.

[14] V. Galindo, "Design of dual reflector antennas with arbitrary phase and amplitude distribution," *IEEE Transactions on Antennas and Propagation*, vol. AP-12, pp. 403–408, July 1964.

[15] B. S. Westcott, F. A. Stevens, and F. Brickell, "GO synthesis of offset dual reflectors," *IEE Proceedings*, vol. 128, pp. 11–18, Feb. 1981.

[16] C. A. Fernandes, "Shaped dielectric lenses for wireless millimeter-wave communications," *IEEE Antennas and Propagation Magazine*, vol. 41, no. 5, pp. 141–150, Oct. 1999.

[17] M. G. M. V. Silveirinha and C. A. Fernandes, "Shaped double-shell dielectric lenses for wireless millimeter wave communications," *Proceedings of 2000 IEEE AP-S International Symposium*, vol. 3, Salt Lake City, UT, July 16–21, 2000, pp. 1674–1677.

[18] D. K. Waineo, "Lens design for arbitrary aperture illumination," *Proceedings of Antennas and Propagation Society International Symposium*, Oct. 11-15, 1976, Amherst, Mass., U.S.A., pp. 476–479.

[19] J. J. Lee, L. I. Parad, and R. S. Chu, "A shaped offset-fed dual-reflector antenna," *IEEE Transactions on Antennas and Propagation*, vol. AP–27, no. 2, pp. 165–171, Mar. 1979.

[20] A. N. Peebles, “A dielectric bifocal lens for multibeam antenna applications,” *IEEE Transactions on Antennas and Propagation*, vol. 36, no. 5, pp. 599–606, May 1988.

[21] J. R. Descardeci and C. G. Parini, “Trireflector compact antenna test range,” *IEE Proceedings Microwaves, Antennas and Propagation*, vol. 144, no. 5, pp. 305–310, Oct. 1997.

[22] J. O. Rubiños-Lòpez and A. Garcia-Píno, “A ray-by-ray algorithm for shaping dual-offset reflector antennas,” *Microwave and Optical Technology Letters*, vol. 15, no. 1, pp. 20–26, May 1997.

[23] J. J. Lee, “Dielectric lens shaping and coma correction zoning, Part 1: Analysis,” *IEEE Transactions on Antennas and Propagation*, AP–31, no. 1, pp. 211–216, Jan. 1983.

[24] J. Häkli, J. Ala-Laurinaho, and A. V. Räisänen, “Numerical synthesis method for designing a shaped dual reflector feed system,” *IEE Proceedings Microwaves, Antennas and Propagation*, vol. 152, no. 5, pp. 311–318, Oct. 2005.

[25] A. Karttunen, *Design of Feed Systems for Hologram-Based Compact Antenna Test Ranges*, Licentiate Thesis, Helsinki University of Technology, Espoo, Finland, 2009, 106 p.

[26] A. P. Pavacic, D. L. del Rio, J. R. Mosig, and G. V. Eleftheriades, “Three-dimensional ray-tracing to model internal reflections in off-axis lens antennas,” *IEEE Transactions on Antennas and Propagation*, vol. 54, no. 2, pp. 604–612, Feb. 2007.

[27] Y. Zhang, J. Wang, Z. Zhao, and J. Yang, “Numerical analysis of dielectric lens antennas using a ray-tracing method and HFSS software,” *IEEE Antennas and Propagation Magazine*, vol. 50, No. 4, pp. 94–101, Aug. 2008.

[28] D. F. Filipovic, S. S. Gearhart, and G. M. Rebeiz, “Double-slot antennas on extended hemispherical and elliptical silicon dielectric lenses,” *IEEE Transactions on Microwave Theory and Techniques*, vol. 41, no. 10, pp. 1738–1749, Oct. 1993.

[29] D. F. Filipovic, G. P. Gauthier, S. Raman, and G. M. Rebeiz, “Off-axis properties of silicon and quartz dielectric lens antennas,” *IEEE Transactions on Antennas and Propagation*, vol. 45, no. 5, pp. 760–766, May 1997.

[30] X. Wu, G. V. Eleftheriades, and T. E. van Deventer-Perkins, "Design and characterization of single- and multiple-beam mm-wave circularly polarized substrate lens antennas for wireless communications," *IEEE Transactions on Microwave Theory and Techniques*, vol. 49, no. 3, pp. 431–441, Mar. 2001.

[31] H.-T. Chou, P. H. Pathak, and R. J. Burkholder, "Application of Gaussian-ray basis functions for the rapid analysis of electromagnetic radiation from reflector antennas," *IEE Proceedings Microwaves, Antennas and Propagation*, vol. 150, no. 3, pp. 177–183, June 2003.

[32] K. K. Chan, S. K. Rao, G. A. Morin, and M. Q. Tang, "Triangular ray-tube analysis of dielectric lens antennas," *IEEE Transactions on Antennas and Propagation*, vol. 45, no. 8, pp. 1277–1285, Aug. 1997.

[33] A. V. Boriskin, G. Godi, R. Sauleau, and A. I. Nosich, "Small hemielliptic dielectric lens antenna analysis in 2-D: boundary integral equations versus geometrical and physical optics," *IEEE Transactions on Antennas and Propagation*, vol. 56, no. 2, pp. 485–492, Feb. 2008.

[34] S. A. Schelkunoff, "On diffraction and radiation of electromagnetic waves," *Physical Review*, vol. 56. pp. 308–316, 1939.

[35] *IEEE Standard Definitions of Terms for Antennas*, IEEE Standard 145-1983, the Institute of Electrical and Electronics Engineers, USA, 1983, 31 p.

[36] J. Tuovinen, A. Vasara, and A. Räisänen, "A new type of compact antenna test range," in *Proceedings of the 22nd European Microwave Conference*, Espoo, Finland, Sept 5–9, 1992, pp. 503–508.

[37] T. Hirvonen, J. Ala-Laurinaho, J. Tuovinen, and A. V. Räisänen, "A compact antenna test range based on a hologram," *IEEE Transactions on Antennas and Propagation*, vol. 45, no. 8, pp. 1270–1276, Aug. 1997.

[38] T. Sehm, J. Ala-Laurinaho, T. Hirvonen, and A. V. Räisänen, "Antenna measurements using a hologram CATR," *Electronics Letters*, vol. 35, no. 10, pp. 757–758, May 1999.

[39] J. Ala-Laurinaho, T. Hirvonen, P. Piironen, A. Lehto, J. Tuovinen, A. V. Räisänen, and U. Frisk, "Measurement of the Odin telescope at 119 GHz with a hologram-type CATR," *IEEE Transactions on Antennas and Propagation*, vol. 49, no. 9, pp. 1264–1270, Sept. 2001.

[40] A. Lönnqvist, T. Koskinen, J. Häkli, J. Säily, J. Ala-Laurinaho, J. Mallat, V. Viikari, J. Tuovinen, and A. V. Räisänen, "Hologram-based compact range for submillimeter-wave antenna testing," *IEEE Transactions on Antennas and Propagation*, vol. 53, no. 10, pp. 3151–3159, Oct. 2005.

[41] J. Häkli, T. Koskinen, A. Lönnqvist, J. Säily, V. Viikari, J. Mallat, J. Ala-Laurinaho, J. Tuovinen, and A. V. Räisänen, "Testing of a 1.5-m reflector antenna at 322 GHz in a CATR based on a hologram," *IEEE Transactions on Antennas and Propagation*, vol. 53, no. 10, pp. 3142–3150, Oct. 2005.

[42] J. Häkli, T. Koskinen, J. Ala-Laurinaho, and A. V. Räisänen, "Dual reflector feed system for hologram-based compact antenna test range," *IEEE Transactions on Antennas and Propagation*, vol. 53, no. 12, pp. 3940–3948, Dec. 2005.

[43] A. D. Olver, "Compact antenna test ranges," *Proceedings of the Seventh International Conference on Antennas and Propagation (ICAP 91)*, April 15–18, 1991, pp. 99–108.

[44] R. C. Johnson, H. A. Ecker, and R. A. Moore, "Compact range techniques and measurements," *IEEE Transactions on Antennas and Propagation*, vol. 17, no. 5, pp. 568–576, Sept. 1969.

[45] J. Hartmann, J. Habersack, H.-J. Steiner, J. Lemanczyk, and P. de Maagt, "Calibration and verification measurements in compensated compact ranges up to 500 GHz," *Proceedings of the 23rd Annual Meeting & Symposium of the Antenna Measurement Techniques Association (AMTA)*, Denver, CO, Oct. 2001, pp. 377–382.

[46] G. A. Woonton, R. B. Borts, and J. A. Caruthers, "Indoor measurements of microwave antenna radiation patterns by means of a metal lens," *Journal of Applied Physics*, vol. 11, pp. 428–430, May 1950.

[47] T. Hirvonen, J. Tuovinen, and A. Räisänen, "Lens-type compact antenna test range at mm-waves," *Proceedings of the 21st European Microwave Conference*, Stuttgart, Germany, 1991, pp. 1079–1083.

[48] W.-H. Lee, "Computer-generated holograms: Techniques and applications," *Progress in Optics XVI, E. Wolf, Ed., Amsterdam, The Netherlands: Elsevier*, pp. 121–231, 1978.

[49] A. Vasara, J. Turunen, and A. T. Friberg, "Realization of general nondiffracting beams with computer-generated holograms," *Journal of Optical Society of America A*, vol. 6, pp. 1748–1754, 1989.

[50] J. Ala-Laurinaho, T. Hirvonen, J. Tuovinen, and A. V. Räisänen, "Numerical modeling of a nonuniform grating with FDTD," *Microwave and Optical Technology Letters*, vol. 15, no. 3, pp. 134–139, June 1997.

[51] J. Ala-Laurinaho, T. Sehm, J. Säily, and A. V. Räisänen, "Cross-polarization performance of the hologram compact antenna test range," *Microwave and Optical Technology Letters*, vol. 27, no. 4, pp. 225–229, Nov. 2000.

[52] T. Koskinen, *Studies on an Amplitude Hologram as the Collimator in a Submillimeter-Wave Compact Antenna Test Range*, Doctoral Thesis, Helsinki University of Technology, Espoo, Finland, 2007.

[53] A. Lönnqvist, J. Mallat, and A. V. Räisänen, "Phase-hologram-based compact RCS test range at 310 GHz for scale models," *IEEE Transactions on Microwave Theory and Techniques*, vol. 54, no. 6, part 1, pp. 2391–2397, June 2006.

[54] A. Lönnqvist, A. Tamminen, J. Mallat, and A. V. Räisänen, "Monostatic reflectivity measurement of radar absorbing materials at 310 GHz," *IEEE Transactions on Microwave Theory and Techniques*, vol. 54, no. 9, pp. 3486–3491, Sept. 2006.

[55] A. Tamminen, A. Lönnqvist, J. Mallat, and A. V. Räisänen, "Monostatic reflectivity and transmittance of radar absorbing materials at 650 GHz," *IEEE Transactions on Microwave Theory and Techniques*, vol. 56, no. 3, pp. 632–637, Mar. 2008.

[56] E. Noponen, A. Tamminen, and M. Vaaja, "Design of transmission-type phase holograms for a compact radar-cross-section measurement range at 650 GHz," *Applied Optics*, vol. 46, no. 20, pp. 4181–4196, Jul. 2007.

[57] T. Koskinen, V. Viikari, J. Häkli, A. Lönnqvist, J. Ala-Laurinaho, J. Mallat, and A. V. Räisänen, "A reflection-type amplitude hologram

as a collimating element in the compact antenna test range," *Proceedings of the 27th Annual Meeting & Symposium of the Antenna Measurement Techniques Association (AMTA)*, Newport, RI, USA, Oct. 30 – Nov. 4, 2005, pp. 417–421.

[58] E. Noponen, J. Häkli, T. Koskinen, A. Lönnqvist, V. Viikari, J. Ala-Laurinaho, J. Mallat, and A. V. Räisänen, "Synthesis of reflector-type phase hologram for compact antenna test range at 310 GHz," *Proceedings of the 4th ESA Workshop on Millimetre-Wave Technology and Applications 8th Topical Symposium on Millimeter Waves – TSMMW2006 7th Millimeter-Wave International Symposium – MINT-MIS2006*, February 15–17, 2006, Espoo, Finland, pp. 391–396.

[59] A. Tamminen, A. Karttunen, M. Vaaja, E. Noponen, J. Ala-Laurinaho, J. Mallat, and A. V. Räisänen, "Reflection-type phase hologram for beam-shaping: experimental results at 310 GHz," *Proceedings of the 30th ESA Antenna Workshop on Antennas for Earth Observation, Science, Telecommunication and Navigation Space Missions*, Noorwijk, The Netherlands, May 27–30, 2008, pp. 470–473.

[60] *IEEE Standard Test Procedure for Antennas*, IEEE Std 149-1979, published by IEEE, Inc., 1979, 143 p., distributed by Wiley-Interscience.

[61] J. Ala-Laurinaho, T. Hirvonen, and A. V. Räisänen, "On the planarity errors of the hologram of the CATR," *IEEE Antennas and Propagation International Symposium*, Orlando, Florida, USA, July 11-16, 1999, pp. 2166–2169.

[62] T. Hirvonen, J. Ala-Laurinaho, and A. V. Räisänen, "Performance analysis of a submillimeter wave hologram CATR," *Proceedings of the 27th European Microwave Conference*, Jerusalem, Israel, Sept. 8-12, 1997, pp. 681-686.

[63] J. Ala-Laurinaho, *Numerical Studies on a Radio Frequency Hologram and its Use in Antenna Measurements*, Doctoral Thesis, Helsinki University of Technology, Espoo, Finland, 2001.

[64] J. Habersack, J. Hartmann, J. Lemanczyk, P. D. Maagt, and H.-J. Steiner, "Facility trade-off for measurements up to 500 GHz,"

Proceedings of the 23rd Annual Meeting & Symposium of the Antenna Measurement Techniques Association (AMTA), Denver, CO, Oct. 2001, pp. 261–266.

[65] J. Hartmann, J. Habersack, H.-J. Steiner, and J. Lemanczyk, "Comparative analysis and measurement of mm-wave applications," *Proceedings of the 4th ESA Workshop on Millimetre-Wave Technology and Applications*, Espoo, Finland, Feb. 15–17, 2006, pp. 429–435.

[66] D. Slater, P. Stek, R. Cofield, R. Dengler, J. Hardy, R. Jarnot, and R. Swindlehurst, "A large aperture 650 GHz near-field measurement system for the earth observing system microwave limb sounder," *Proceedings of the 23rd Annual Meeting & Symposium of the Antenna Measurement Techniques Association (AMTA)*, Denver, CO., USA, Oct. 21-26, 2001, pp. 468 – 473.

[67] T. Manabe, T. Nishibori, K. Mizukoshi, F. Otsubo, S. Ochiai, and H. Ohmine, "Measurement of the offset-cassegrain antenna of JEM/SMILES using a near-field phase-retrieval method in the 640-GHz band," *IEEE Transactions on Antennas and Propagation*, vol. 60, no. 8, pp. 3971–3976, Aug. 2012.

[68] T. Koskinen, J. Ala-Laurinaho, J. Säily, A. Lönnqvist, J. Häkli, J. Mallat, J. Tuovinen, and A. V. Räisänen, "Experimental study on a hologram-based compact antenna test range at 650 GHz," *IEEE Transactions on Microwave Theory and Techniques*, vol. 53, no. 9, pp. 2999–3006, Sept. 2005.

[69] T. Koskinen, J. Häkli, J. Ala-Laurinaho, A. Lönnqvist, V. Viikari, J. Mallat, and A. V. Räisänen, "Study on the dual polarized operation of the hologram based compact antenna test range," *Proceedings of the 28th ESA Antenna Workshop on Space Antenna Systems and Technologies*, ESTEC, Noordwijk, The Netherlands, May 31 – June 3, 2005, pp. 401–406.

[70] T. Koskinen, J. Ala-Laurinaho, J. Häkli, and A. V. Räisänen, "Studies on an amplitude hologram as a submillimeter-wave collimator at circular polarisation," *Proceedings of the European Conference on Antennas and Propagation (EuCAP)*, Nice, France, Nov. 6–10, 2006.

[71] K. Pontoppidan, *Technical Description of GRASP8*, Ticra engineering consultants, 2003, 376 p.

[72] M. Vaaja, J. Häkli, J. Mallat, and A. V. Räisänen, “Assesment of a planar near-field range for quiet-zone measurements at 650 GHz,” *Proceedings of the 29th Annual Meeting & Symposium of the Antenna Measurement Techniques Association (AMTA)*, St. Louis, MO, USA, Nov. 4–9, 2007, p. A07-0061.

[73] J. Hartmann, J. Habersack, and H.-J. Steiner, “Improvement and validation of design tools for antennas of space instruments working in terahertz frequency range,” *Proceedings of the 3rd European Conference on Antennas and Propagation (EuCAP 2009)*, Berlin, Germany, March 23–27, 2009, pp. 2433–2436.

[74] D. B. Rutledge and M. S. Muha, “Imaging antenna arrays,” *IEEE Transactions on Antennas and Propagation*, vol. 30, no. 4, pp. 535–540, July 1982.

[75] G. M. Rebeiz, “Millimeter-wave and terahertz integrated circuit antennas,” *Proceedings of the IEEE*, vol. 80, no. 11, pp. 1748–1770, Nov. 1992.

[76] M. J. M. van der Vorst, P. J. I. de Maagt, and M. H. A. J. Herben, “Scan-optimized integrated lens antennas," *27th European Microwave Conference*, Jerusalem, Israel, 1997, pp. 605–610.

[77] M. J. M. van der Vorst, P. J. I. de Maagt, and M. H. A. J. Herben, “Effect of internal reflections on the radiation properties and input admittance of integrated lens antennas," *IEEE Transactions on Microwave Theory and Techniques*, vol. 47, no. 9, pp. 1696–1704, Sept. 1999.

[78] M. J. M. van der Vorst, P. J. I. de Maagt, A. Neto, A. L. Ryenolds, R. M. Heeres, W. Luinge, and M. H. A. J. Herben, “Effect of internal reflections on the radiation properties and input admittance of integrated lens antennas—comparison between measurements and theory," *IEEE Transactions on Microwave Theory and Techniques*, vol. 49, no. 6, pp. 1118–1125, June 2001.

[79] A. Neto, A. Toccafondi, and S. Maci, “Mutual coupling between slots printed at the back of elliptical dielectric lenses,” *IEEE Transactions on Microwave Theory and Techniques*, vol. 49, no. 6, pp. 1118–1125, 2001.

[80] A. V. Boriskin, R. Sauleau, and A. I. Nosich, “Performance of hemielliptic dielectric lens antennas with optimal edge illumination," *IEEE Transactions on Antennas and Propagation*, vol. 57, no. 7, pp. 2193–2198, July 2009.

[81] N. Llombart G. Chattopadhyay, A. Skalare, and I. Mehdi, “Novel terahertz antenna based on a silicon lens fed by a leaky wave enhanced waveguide," *IEEE Transactions on Antennas and Propagation*, vol. 59, no. 6, pp. 2160–2168, June 2011.

[82] A. Artemenko, A. Maltsev, R. Maslennikov, A. Sevastyanov, and V. Ssorin, “Beam steerable quartz integrated lens antenna for 60 GHz frequency band,” *European Conference on Antennas and Propagation (EuCAP)*, Rome, Italy, Apr. 11–15, 2011, pp. 788–792.

[83] A. Artemenko, A. Maltsev, A. Mozharovskiy, A. Sevastyanov, V. Ssorin, and R. Maslennikov, “Millimeter-wave electronically steerable integrated lens antennas for WLAN/WPAN applications," *IEEE Transactions on Antennas and Propagation*, vol. 61, no. 4, pp. 1665–1671, April 2013.

[84] A. C. Ludwig, “The definition of cross polarization,” *IEEE Transactions on Antennas and Propagation*, vol. AP-21, no. 1, pp. 116–119, Jan. 1973.

[85] D. Bourreau, A. Péden, and S. Le Maguer, “A quasi-optical free-space measurement setup without time-domain gating for material characterization in the W-band," *IEEE Transactions on Instrumentation and Measurement*, vol. 55, no. 6, pp. 2022–2028, Dec. 2006.

Errata

Publication VIII

In Section IV.A the largest feed offset of port 1 is 40 mm, not 45 mm.

Publication XI

In Section 4 $\Delta_{3dB}/d_{e\,min}$ should read $\Delta_{3dB}/d_{e\,max}$.

The millimetre and submillimetre wave frequency ranges have many current and potential applications for example in satellite technology and telecommunications. This thesis contributes to the design of electrically large reflector and lens antennas using ray tracing.
In the first part of the thesis, a dual reflector feed system is designed with a ray-tracing synthesis method for a hologram-based compact antenna test range.
In the second part of the thesis, several beam-steering integrated lens antennas are designed with ray-tracing based antenna simulations.
Several antennas are designed and tested with antenna measurements in order to study and verify the novel antenna design methods presented in this thesis.

Aalto-DD 127/2013

ISBN 978-952-60-5292-2
ISBN 978-952-60-5293-9 (pdf)
ISSN-L 1799-4934
ISSN 1799-4934
ISSN 1799-4942 (pdf)

Aalto University
School of Electrical Engineering
Department of Radio Science and Engineering
www.aalto.fi